6-10-2019

The Effect Of Binarity On Circumstellar Disk Evolution

S. A. Barenfeld

J. M. Carpenter

A. I. Sargent

See next page for additional authors

Authors

S. A. Barenfeld, J. M. Carpenter, A. I. Sargent, A. C. Rizzuto, A. L. Kraus, T. Meshkat, R. L. Akeson, Eric L.N. Jensen, and S. Hinkley

The Effect of Binarity on Circumstellar Disk Evolution

Scott A. Barenfeld[1] , John M. Carpenter[2] , Anneila I. Sargent[1], Aaron C. Rizzuto[3] , Adam L. Kraus[3] , Tiffany Meshkat[4,5] ,
Rachel L. Akeson[6] , Eric L. N. Jensen[7] , and Sasha Hinkley[8]

[1] California Institute of Technology, Department of Astronomy, MC 249-17, Pasadena, CA 91125, USA
[2] Joint ALMA Observatory, Av. Alonso de Córdova 3107, Vitacura, Santiago, Chile
[3] The University of Texas at Austin, Department of Astronomy, Austin, TX 78712, USA
[4] IPAC, Caltech, M/C 100-22, 1200 East California Boulevard, Pasadena, CA 91125, USA
[5] Jet Propulsion Laboratory, California Institute of Technology, 4800 Oak Grove Drive, Pasadena, CA 91109, USA
[6] IPAC-NExScI, Caltech, Pasadena, CA 91125, USA
[7] Swarthmore College, Department of Physics & Astronomy, 500 College Avenue, Swarthmore, PA 19081-1390, USA
[8] University of Exeter, Physics Department, Stocker Road, Exeter, EX4 4QL, UK
Received 2018 August 30; revised 2019 April 28; accepted 2019 April 29; published 2019 June 12

Abstract

We present new results on how the presence of stellar companions affects disk evolution based on a study of the 5–11 Myr old Upper Scorpius OB Association. Of the 50 G0-M3 Upper Sco members with disks in our sample, only seven host a stellar companion within $2''$ and brighter than $K = 15$, compared to 35 of 75 members without disks. This matches a trend seen in the 1–2 Myr old Taurus region, where systems with a stellar companion within 40 au have a lower fraction of infrared-identified disks than those without such companions, indicating shorter disk lifetimes in close multiple systems. However, the fractions of disk systems with a stellar companion within 40 au match in Upper Sco and Taurus. Additionally, we see no difference in the millimeter brightnesses of disks in Upper Sco systems with and without companions, in contrast to Taurus where systems with a companion within 300 au are significantly fainter than wider and single systems. These results suggest that the effects of stellar companions on disk lifetimes occur within the first 1–2 Myr of disk evolution, after which companions play little further role. By contrast, disks around single stars lose the millimeter-sized dust grains in their outer regions between ages of 1–2 Myr and 5–11 Myr. The end result of small dust disk sizes and faint millimeter luminosities is the same whether the disk has been truncated by a companion or has evolved through internal processes.

Key words: binaries: general – open clusters and associations: individual (Upper Scorpius OB1) – protoplanetary disks – stars: pre-main sequence

1. Introduction

The formation and evolution of circumstellar disks is fundamental to our understanding of planet formation. This process begins with the collapse of a dense molecular cloud core and the subsequent formation of a protostar surrounded by an infalling envelope. Over a period of about 1 Myr, conservation of angular momentum causes the infalling material to form a circumstellar disk which remains around the star after the surrounding envelope is lost (Li et al. 2014 and references therein). This disk can provide the material for planet formation, a process that is not fully understood but likely involves direct collapse of disk material into a planet through gravitational instability and/or the slower growth of planetesimals and planets through core accretion (e.g., Chabrier et al. 2014; Helled et al. 2014). As the disk evolves, material will continue to viscously accrete onto the central star (e.g., Hartmann et al. 1998). At the same time, photoevaporation from the disk surface by high-energy stellar radiation dissipates disk material (Owen et al. 2012; Alexander et al. 2014; Gorti et al. 2015). Simultaneously, dust grains migrate inwards due to gas drag and grow to form larger bodies, depleting the small grain population (Whipple 1972; Weidenschilling 1977; Brauer et al. 2007; Birnstiel & Andrews 2014; Testi et al. 2014). By an age of 5–10 Myr, the majority of disks have dissipated (Hernández et al. 2008), leaving behind a young star surrounded by any planets and associated debris that have formed.

Even for single stars, there are many uncertainties associated with the processes of disk evolution and planet formation.

Additional complications arise from the fact that most stars are born in multiple systems. Studies of field stars show that the fraction of multiple systems is ∼50% among solar-type stars (Raghavan et al. 2010) and ∼30%–40% for later-type stars (Fischer & Marcy 1992; Bergfors et al. 2010). In the pre-main-sequence phase, multiplicity is at least as common (Ratzka et al. 2005; Kraus et al. 2008, 2011; Lafrenière et al. 2008; Cheetham et al. 2015). Indeed, surveys of the earliest protostars indicate that a high binary fraction is intrinsic to the star formation process (Chen et al. 2013). Results from the *Kepler* survey (Borucki et al. 2010) show that while planet formation is suppressed in binary systems (Wang et al. 2014a, 2014b, 2015a, 2015b; Kraus et al. 2016), it is possible for such planets to form (e.g., Holman & Wiegert 1999; Dupuy et al. 2016; Hirsch et al. 2017). A complete understanding of the formation and evolution of stars and planets must therefore take the effects of stellar companions into account.

Theoretical calculations have long predicted that the presence of a stellar companion will have an important influence on disk evolution (Papaloizou & Pringle 1977). A disk around a single component of a binary system will be tidally truncated at approximately one-third to one-half of the binary separation and the resulting smaller disk will dissipate on a more rapid timescale than an unperturbed disk around a single star (e.g., Artymowicz & Lubow 1994; Pichardo et al. 2005; Jang-Condell 2015). In fact, some initial surveys found that the fraction of binaries is lower in systems with disks and, in particular, accreting disks (Ghez et al. 1993; Ratzka et al. 2005), although other studies found no difference between

accreting and non-accreting systems (Leinert et al. 1993; Kohler & Leinert 1998). Most recently, catalogs of much larger samples of disks identified with the *Spitzer Space Telescope* (Werner et al. 2004) and the *Wide-field Infrared Survey Explorer* (*WISE*; Wright et al. 2010) have provided more convincing evidence that the presence of stellar companions leads to shorter disk lifetimes (Bouwman et al. 2006; Daemgen et al. 2016; Long et al. 2018), with the disk fraction in 1–3 Myr old close binary systems ($\leqslant 40$ au separation) less than half that of wider binaries and single stars (Cieza et al. 2009; Kraus et al. 2012; Cheetham et al. 2015).

Submillimeter interferometric observations are now providing high-resolution images of the outer regions of disks, where most of the material resides, so that the effects of binarity on the entire disk, beyond the central regions probed by infrared observations, can be studied. In a millimeter study of 1–2 Myr old disks in Taurus, Harris et al. (2012) detected only one-third of disks in binary systems compared to two-thirds of single-star disks. In addition, the authors observed a positive correlation between binary separation and disk millimeter luminosity. While disks in binary systems with separations greater than 300 au had luminosities indistinguishable from single stars, disks in systems with a companion between 30 and 300 au were fainter by a factor of five. Disks in systems with a companion within 30 au were an additional factor of five fainter, implying that even in Taurus binary systems that maintain their disks, a substantial fraction of the millimeter-wavelength-emitting grains are lost due to the companion (see also Jensen et al. 1994, 1996).

Understanding how stellar companions affect later stages of disk evolution requires observations of older systems. Since these older disks are significantly fainter than their younger counterparts (Nuernberger et al. 1997; Carpenter 2002; Lee et al. 2011; Mathews et al. 2012; Williams et al. 2013; Carpenter et al. 2014; Ansdell et al. 2015; Barenfeld et al. 2016), detailed studies require the sensitivity of the Atacama Large Millimeter/submillimeter Array (ALMA). To this end, we measured the properties of over 100 disks in the 5–11 Myr old Upper Scorpius OB Association (hereafter Upper Sco) using ALMA and found that these disks are a factor of ~4.5 less massive (Barenfeld et al. 2016) and a factor of ~3 smaller (Barenfeld et al. 2017) than their younger counterparts. In this paper, we consider how the influence of stellar companions has impacted the evolution of these disks to their current state. To investigate this, we searched for companions to the stars in our Upper Sco disk sample using adaptive optics (AO) imaging and aperture masking. We describe our sample, observations, and data reduction in Section 2. Section 3 specifies how companions were identified. In Section 4 we describe our detected companions and compare the companion frequency of systems with and without disks in Upper Sco. In Section 5, we discuss how the effects of stellar multiplicity on disk properties vary with age in the context of disk evolution. Our conclusions are summarized in Section 6.

2. Sample and Observations

Our sample contains all 100 Upper Sco stars with spectral types between G2 and M4.75 (inclusive) as well as 13 M5 stars in Upper Sco identified as hosting disks by Carpenter et al. (2006) and Luhman & Mamajek (2012).[9] These disks were

---

[9] Recent surveys, published after the present observations were obtained, have since expanded the known population of stars and disks in Upper Sco (Esplin et al. 2018; Luhman et al. 2018).

discovered based on excess infrared emission observed by *Spitzer* and *WISE* and include 82 disks classified as "full," "evolved," or "transitional" by Luhman & Mamajek (2012) based on their infrared colors. We consider these disks to be "primordial," i.e., a direct evolution of younger protoplanetary disks such as those in Taurus. The remaining 31 disks in the sample are characterized as "debris/evolved transitional" (Luhman & Mamajek 2012). These disks may represent the final phase of primordial disk evolution or be second-generation objects composed of dust created by the collision of planetesimals, with only an indirect evolutionary link to younger disks. The full sample is listed in Table 1 and receives a more detailed description in Barenfeld et al. (2016). Distances to the stars in the sample are taken from the catalog of Bailer-Jones et al. (2018), inferred from *Gaia* parallaxes using a Bayesian distance prior.

Twenty-seven systems in our sample have already been surveyed for stellar companions. These systems are listed in Table 2, along with the properties of any known companions. We obtained AO imaging and aperture masking observations of the remaining 86 stars using the NIRC2 AO imager (instrument PI: Keith Matthews) on the 10 m Keck II telescope. Targets were observed on the nights of 2011 May 15, 2013 May 30–31, and 2015 May 27–28. Sources brighter than $R = 13.5$ were observed using natural guide star tip-tilt correction. Otherwise, a laser guide star was used (Wizinowich et al. 2006).

Based on the Kraus et al. (2008) multiplicity survey of Upper Sco systems without disks identified by Luhman & Mamajek (2012), we expected to detect stellar companions at separations ranging from tens of milliarcseconds to several arcseconds. This range of separations can be probed using a combination of AO imaging, able to detect medium and wide separation companions, and nonredundant aperture masking, which achieves deeper contrast limits than AO imaging within a few hundred milliarcseconds. We thus observed our sample with both techniques using NIRC2. Our observing procedure for each of these techniques is described below.

2.1. Imaging Observations

Our imaging observations are summarized in Table 1. For targets observed in 2013 and 2015, we acquired two 10 s AO images using either the K' or K_c filter on NIRC2. Targets with a Two Micron All Sky Survey (2MASS; Cutri et al. 2003; Skrutskie et al. 2006) magnitude brighter than $K_s = 8.3$ were observed using the K_c filter to prevent saturation. A third 10 s image was obtained of targets with a visually identifiable companion. If no such companion was seen, we obtained two further frames of 20 s AO images with the K' filter. These additional frames used a 600 mas diameter coronagraph for targets brighter than 2MASS $K_s = 10.6$ that would be partially visible behind the semi-transparent coronagraph. Fainter targets were observed without the coronagraph, allowing us to easily determine primary positions when calculating companion separations. Due to unknown errors during observations, the two initial 10 s images were not saved on the nights of 2015 May 27–28, reducing the total integration times shown in Table 1. To avoid saturation in the initial and follow-up frames, we used shorter exposure times that were coadded to give the final 10 and 20 s frames. The exposure time per coadd was set based on the 2MASS K_s magnitude of the target and the number of coadds was chosen to give total integration times of

Table 1
Upper Sco Disk Sample

Source	Disk Type	Spectral Type	K (mag)	Distance[a] (pc)	$S_{0.88\,mm}$ [b] (mJy)	Observation Epoch[c]	Integration Time (s)		Coronagraph?
							Imaging	Masking[d]	
2MASS J15354856-2958551	primordial	M4	9.46 ± 0.03	145 (−11, +11)	1.92 ± 0.15	⋯	⋯	⋯	⋯
2MASS J15514032-2146103	primordial	M4	11.00 ± 0.02	142 (−2, +2)	0.76 ± 0.16	2013 May 30	60	120	no
2MASS J15521088-2125372	primordial	M4	12.08 ± 0.03	167 (−7, +8)	−0.10 ± 0.15	2015 May 27	40	160	no
2MASS J15530132-2114135	primordial	M4	11.02 ± 0.02	146 (−2, +3)	5.78 ± 0.14	2013 May 30	60	120	no
2MASS J15534211-2049282	primordial	M3.4	9.62 ± 0.03	135 (−3, +3)	2.93 ± 0.29	2013 May 30	30	⋯	no
2MASS J15551704-2322165	debris/ev. trans.	M2.5	9.33 ± 0.02	124 (−2, +2)	0.11 ± 0.15	2015 May 27	40	160	yes
2MASS J15554883-2512240	debris/ev. trans.	G3	8.29 ± 0.02	143 (−1, +1)	−0.14 ± 0.15	2015 May 27	40	320	yes
2MASS J15562477-2225552	primordial	M4	10.79 ± 0.02	141 (−2, +2)	0.28 ± 0.18	2013 May 30	60	120	no
2MASS J15570641-2206060	primordial	M4	11.29 ± 0.03	157 (−3, +3)	0.32 ± 0.20	2013 May 30	60	120	no
2MASS J15572986-2258438	primordial	M4	11.19 ± 0.02	145 (−11, +11)	−0.04 ± 0.20	2013 May 30	30	⋯	no
2MASS J15581270-2328364	debris/ev. trans.	G6	8.02 ± 0.02	143 (−1, +1)	0.00 ± 0.15	2015 May 27	40	160	yes
2MASS J15582981-2310077	primordial	M3	11.30 ± 0.02	147 (−3, +3)	5.86 ± 0.18	2013 May 30	60	120	no
2MASS J15583692-2257153	primordial	G7	7.05 ± 0.03	165 (−4, +4)	174.92 ± 0.27	⋯	⋯	⋯	⋯
2MASS J15584772-1757595	debris/ev. trans.	K4	8.32 ± 0.02	138 (−1, +1)	−0.20 ± 0.15	2015 May 27	40	320	yes
2MASS J16001330-2418106	debris/ev. trans.	M0	9.51 ± 0.02	146 (−1, +1)	0.05 ± 0.15	⋯	⋯	⋯	⋯
2MASS J16001730-2236504	primordial	M4	9.94 ± 0.02	148 (−2, +2)	0.10 ± 0.15	2015 May 27	40	160	yes
2MASS J16001844-2230114	primordial	M4.5	10.41 ± 0.02	138 (−8, +9)	3.89 ± 0.15	2015 May 27	40	160	yes
2MASS J16014086-2258103	primordial	M4	9.85 ± 0.02	124 (−2, +2)	3.45 ± 0.14	⋯	⋯	⋯	⋯
2MASS J16014157-2111380	primordial	M4	11.68 ± 0.03	144 (−2, +3)	0.66 ± 0.14	2013 May 31	60	120	no
2MASS J16020039-2221237	debris/ev. trans.	M1	8.84 ± 0.02	144 (−2, +3)	−0.08 ± 0.14	⋯	⋯	⋯	⋯
2MASS J16020287-2236139[e]	debris/ev. trans.	M0	11.61 ± 0.03	145 (−11, +11)	0.04 ± 0.15	2015 May 28	60	⋯	no
2MASS J16020757-2257467	primordial	M2.5	9.86 ± 0.02	140 (−1, +1)	5.26 ± 0.27	2013 May 31	40	120	yes
2MASS J16024152-2138245	primordial	M4.75	11.18 ± 0.02	141 (−2, +3)	10.25 ± 0.19	2013 May 31	60	120	no
2MASS J16025123-2401574	debris/ev. trans.	K4	8.93 ± 0.02	143 (−1, +1)	0.07 ± 0.15	⋯	⋯	⋯	⋯
2MASS J16030161-2207523	primordial	M4.75	11.73 ± 0.02	144 (−3, +4)	2.81 ± 0.12	2015 May 27	40	160	no
2MASS J16031329-2112569	primordial	M4.75	11.16 ± 0.02	143 (−2, +2)	0.06 ± 0.12	2015 May 27	40	160	no
2MASS J16032225-2413111	primordial	M3.5	10.01 ± 0.02	144 (−3, +3)	2.42 ± 0.15	2013 May 30	40	120	yes
2MASS J16033471-1829303	primordial	M5	11.48 ± 0.02	146 (−7, +8)	⋯	2013 May 30	30	⋯	no
2MASS J16035767-2031055	primordial	K5	8.37 ± 0.03	142 (−1, +1)	4.30 ± 0.39	⋯	⋯	⋯	⋯
2MASS J16035793-1942108	primordial	M2	10.32 ± 0.02	157 (−2, +2)	1.17 ± 0.14	2013 May 30	40	120	yes
2MASS J16041740-1942287	primordial	M3.5	10.42 ± 0.05	161 (−2, +2)	0.89 ± 0.14	2013 May 31	30	⋯	no
2MASS J16042165-2130284	primordial	K2	8.51 ± 0.02	149 (−1, +1)	218.76 ± 0.81	⋯	⋯	⋯	⋯
2MASS J16043916-1942459	debris/ev. trans.	M3.25	10.79 ± 0.02	151 (−2, +2)	0.49 ± 0.15	2015 May 28	40	160	yes
2MASS J16050231-1941554[e]	debris/ev. trans.	M4.5	11.54 ± 0.02	157 (−3, +3)	−0.16 ± 0.15	2015 May 28	40	160	no
2MASS J16052459-1954419[e]	debris/ev. trans.	M3.5	10.48 ± 0.02	152 (−2, +2)	0.22 ± 0.15	2015 May 28	40	160	no
2MASS J16052556-2035397	primordial	M5	11.05 ± 0.02	142 (−3, +3)	1.53 ± 0.20	2013 May 30	30	⋯	no
2MASS J16052661-1957050	primordial	M4.5	10.69 ± 0.02	145 (−11, +11)	0.07 ± 0.15	2013 May 31	30	⋯	no
2MASS J16053215-1933159	primordial	M5	11.36 ± 0.02	154 (−2, +3)	0.25 ± 0.20	2013 May 30	60	120	no
2MASS J16054540-2023088	primordial	M2	10.41 ± 0.02	145 (−2, +2)	7.64 ± 0.15	2013 May 30	30	⋯	no
2MASS J16055863-1949029	primordial	M4	10.74 ± 0.02	148 (−2, +2)	−0.08 ± 0.15	2015 May 28	40	160	yes
2MASS J16060061-1957114	primordial	M5	10.44 ± 0.03	145 (−11, +11)	0.00 ± 0.13	2013 May 30	30	⋯	no
2MASS J16061144-1935405	primordial	M5	11.78 ± 0.02	139 (−3, +3)	⋯	2013 May 30	60	⋯	no
2MASS J16061330-2212537	debris/ev. trans.	M4	9.59 ± 0.02	139 (−2, +2)	−0.20 ± 0.12	2015 May 28	40	160	yes
2MASS J16062196-1928445	primordial	M0	8.62 ± 0.03	145 (−11, +11)	4.08 ± 0.52	⋯	⋯	⋯	⋯
2MASS J16062277-2011243	primordial	M5	11.00 ± 0.02	151 (−2, +2)	0.59 ± 0.14	2013 May 30	60	⋯	no
2MASS J16063539-2516510	primordial	M4.5	11.71 ± 0.03	139 (−3, +3)	1.69 ± 0.15	2013 May 30	60	⋯	no

Table 1
(Continued)

Source	Disk Type	Spectral Type	K (mag)	Distance[a] (pc)	S$_{0.88 mm}$[b] (mJy)	Observation Epoch[c]	Integration Time (s)		Coronagraph?
							Imaging	Masking[d]	
2MASS J16064102-2455489[e]	primordial	M4.5	12.07 ± 0.02	152 (−3, +3)	3.05 ± 0.14	2015 May 28	40	160	no
2MASS J16064115-2517044	primordial	M3.25	10.92 ± 0.02	149 (−2, +2)	0.20 ± 0.15	2013 May 31	60	120	no
2MASS J16064385-1908056	primordial	K6	9.20 ± 0.02	144 (−6, +7)	0.84 ± 0.15	⋯	⋯	⋯	⋯
2MASS J16070014-2033092	primordial	M2.75	9.94 ± 0.02	139 (−2, +2)	0.22 ± 0.15	2013 May 31	40	⋯	yes
2MASS J16070211-2019387	primordial	M5	11.40 ± 0.03	149 (−5, +5)	−0.09 ± 0.20	⋯	⋯	⋯	⋯
2MASS J16070873-1927341	debris/ev. trans.	M4	11.17 ± 0.02	146 (−2, +2)	−0.09 ± 0.15	2011 May 15	90	940	no
2MASS J16071971-2020555	debris/ev. trans.	M3	10.72 ± 0.02	164 (−3, +3)	0.16 ± 0.16	2011 May 15	90	1200	no
2MASS J16072625-2432079	primordial	M3.5	9.88 ± 0.02	142 (−2, +2)	13.12 ± 0.24	2013 May 30	40	⋯	yes
2MASS J16072747-2059442	primordial	M4.75	10.22 ± 0.02	145 (−11, +11)	2.13 ± 0.12	2013 May 31	30	⋯	no
2MASS J16073939-1917472	debris/ev. trans.	M2	9.80 ± 0.02	137 (−1, +1)	0.58 ± 0.16	2011 May 15	90	800	no
2MASS J16075796-2040087	primordial	M1	7.81 ± 0.02	198 (−8, +8)	23.49 ± 0.12	2015 May 28	40	160	yes
2MASS J16080555-2218070	debris/ev. trans.	M3.25	9.85 ± 0.02	142 (−1, +1)	0.02 ± 0.12	2015 May 28	40	160	yes
2MASS J16081566-2222199	primordial	M3.25	9.95 ± 0.02	140 (−2, +2)	0.97 ± 0.12	2013 May 31	40	120	yes
2MASS J16082324-1930009	primordial	K9	9.47 ± 0.02	137 (−1, +1)	43.19 ± 0.81	⋯	⋯	⋯	⋯
2MASS J16082733-2217292	primordial	M5	10.45 ± 0.02	146 (−3, +3)	⋯	2013 May 31	40	120	yes
2MASS J16082751-1949047	primordial	M5	10.59 ± 0.02	145 (−11, +11)	0.76 ± 0.13	2013 May 30	30	⋯	no
2MASS J16082870-2137198	primordial	M5	10.76 ± 0.02	139 (−2, +2)	⋯	2013 May 31	60	120	no
2MASS J16083455-2211559	primordial	M4.5	11.53 ± 0.02	135 (−3, +3)	0.01 ± 0.12	2013 May 31	60	120	no
2MASS J16084894-2400045	primordial	M3.75	10.94 ± 0.02	144 (−2, +2)	−0.06 ± 0.15	2013 May 30	60	⋯	no
2MASS J16090002-1908368	primordial	M5	10.96 ± 0.02	139 (−3, +3)	1.73 ± 0.13	2013 May 30	60	120	no
2MASS J16090075-1908526	primordial	K9	9.15 ± 0.03	137 (−1, +1)	47.28 ± 0.91	⋯	⋯	⋯	⋯
2MASS J16093558-1828232	primordial	M3	10.70 ± 0.02	165 (−3, +3)	0.69 ± 0.15	2013 May 31	60	120	no
2MASS J16094098-2217594	debris/ev. trans.	M0	8.44 ± 0.03	146 (−1, +1)	0.44 ± 0.12	⋯	⋯	⋯	⋯
2MASS J16095361-1754474	primordial	M3	11.53 ± 0.02	157 (−5, +6)	0.87 ± 0.16	2013 May 30	60	120	no
2MASS J16095441-1906551	debris/ev. trans.	M1	9.60 ± 0.02	136 (−1, +1)	0.50 ± 0.16	⋯	⋯	⋯	⋯
2MASS J16095933-1800090	primordial	M4	10.34 ± 0.02	136 (−2, +2)	0.67 ± 0.18	2013 May 30	40	120	yes
2MASS J16101473-1919095	debris/ev. trans.	M2	10.03 ± 0.02	139 (−1, +2)	0.01 ± 0.16	2011 May 15	90	1400	no
2MASS J16101888-2502325	primordial	M4.5	11.26 ± 0.05	155 (−4, +4)	0.30 ± 0.14	2015 May 28	40	160	no
2MASS J16102174-1904067	debris/ev. trans.	M1	9.62 ± 0.02	133 (−1, +1)	−0.05 ± 0.16	⋯	⋯	⋯	⋯
2MASS J16102819-1910444[f]	primordial	M4	11.79 ± 0.02	150 (−2, +3)	0.05 ± 0.16	2013 May 31	40	120	yes
2MASS J16102857-1904469	primordial	M3	8.71 ± 0.02	145 (−11, +11)	0.66 ± 0.16	⋯	⋯	⋯	⋯
2MASS J16103956-1916524[e]	debris/ev. trans.	M2	10.27 ± 0.03	158 (−2, +2)	0.07 ± 0.16	2015 May 28	40	160	yes
2MASS J16104202-2101319	debris/ev. trans.	K5	8.56 ± 0.03	139 (−1, +1)	0.17 ± 0.12	⋯	⋯	⋯	⋯
2MASS J16104636-1840598	primordial	M4.5	11.27 ± 0.02	143 (−3, +3)	1.78 ± 0.16	2015 May 28	40	160	no
2MASS J16111330-2019029	primordial	M3	9.56 ± 0.03	155 (−1, +2)	4.88 ± 0.16	2013 May 31	40	120	yes
2MASS J16111534-1757214	primordial	M1	9.20 ± 0.02	136 (−1, +1)	0.18 ± 0.16	⋯	⋯	⋯	⋯
2MASS J16111705-2213085	primordial	M5	10.58 ± 0.02	146 (−3, +3)	⋯	2013 May 31	60	120	no
2MASS J16112057-1820549	debris/ev. trans.	K5	8.56 ± 0.02	136 (−1, +1)	−0.06 ± 0.16	⋯	⋯	⋯	⋯
2MASS J16113134-1838259	primordial	K5	5.78 ± 0.02	127 (−2, +2)	903.56 ± 0.85	⋯	⋯	⋯	⋯
2MASS J16115091-2012098	primordial	M3.5	10.40 ± 0.02	152 (−4, +4)	0.66 ± 0.16	2013 May 31	40	120	yes
2MASS J16122737-2009596	primordial	M4.5	11.54 ± 0.02	147 (−4, +4)	0.53 ± 0.16	2015 May 28	40	160	no
2MASS J16123916-1859284	primordial	M0.5	9.11 ± 0.03	139 (−2, +2)	6.01 ± 0.29	2013 May 31	40	120	yes
2MASS J16124893-1800525[e]	debris/ev. trans.	M3	10.36 ± 0.02	158 (−2, +2)	0.11 ± 0.16	2015 May 28	60	160	no
2MASS J16125533-2319456	debris/ev. trans.	G2	7.29 ± 0.02	151 (−1, +1)	0.08 ± 0.13	2015 May 28	40	160	yes
2MASS J16130996-1904269	primordial	M4	10.58 ± 0.02	137 (−2, +2)	−0.05 ± 0.16	2013 May 31	60	120	no

Table 1
(Continued)

Source	Disk Type	Spectral Type	K (mag)	Distance[a] (pc)	$S_{0.88\,mm}$[b] (mJy)	Observation Epoch[c]	Integration Time (s) Imaging	Masking[d]	Coronagraph?
2MASS J16133650-2503473	primordial	M3.5	10.26 ± 0.02	145 (−11, +11)	0.88 ± 0.19	2013 May 30	30	⋯	no
2MASS J16135434-2320342	primordial	M4.5	10.06 ± 0.02	145 (−11, +11)	7.53 ± 0.13	2013 May 31	30	⋯	no
2MASS J16141107-2305362	primordial	K2	7.46 ± 0.03	145 (−11, +11)	4.77 ± 0.14	⋯	⋯	⋯	⋯
2MASS J16142029-1906481	primordial	M0	7.81 ± 0.03	142 (−2, +3)	40.69 ± 0.22	⋯	⋯	⋯	⋯
2MASS J16142893-1857224	debris/ev. trans.	M2.5	9.47 ± 0.02	141 (−2, +2)	0.10 ± 0.16	2015 May 28	40	160	yes
2MASS J16143367-1900133	primordial	M3	8.26 ± 0.02	141 (−2, +2)	1.24 ± 0.16	2013 May 31	40	120	yes
2MASS J16145918-2750230	debris/ev. trans.	G8	8.69 ± 0.02	145 (−11, +11)	0.03 ± 0.19	2015 May 28	40	160	yes
2MASS J16145928-2459308	primordial	M4.25	11.09 ± 0.02	158 (−3, +3)	−0.03 ± 0.12	2013 May 30	100	⋯	no
2MASS J16151239-2420091	primordial	M4	12.13 ± 0.02	153 (−3, +3)	0.22 ± 0.12	2013 May 30	60	⋯	no
2MASS J16153456-2242421	primordial	M0	7.91 ± 0.02	139 (−1, +1)	11.75 ± 0.12	⋯	⋯	⋯	⋯
2MASS J16154416-1921171	primordial	K5	8.40 ± 0.02	131 (−2, +2)	23.57 ± 0.16	2013 May 31	40	120	yes
2MASS J16163345-2521505	primordial	M0.5	10.13 ± 0.02	162 (−1, +1)	2.88 ± 0.30	2013 May 31	40	120	yes
2MASS J16181618-2619080	primordial	M4.5	10.94 ± 0.02	145 (−11, +11)	−0.07 ± 0.12	⋯	⋯	⋯	⋯
2MASS J16181904-2028479	primordial	M4.75	10.96 ± 0.02	137 (−2, +2)	4.62 ± 0.12	2013 May 30	60	⋯	no
2MASS J16215466-2043091	debris/ev. trans.	K7	9.15 ± 0.02	109 (−1, +1)	0.49 ± 0.12	⋯	⋯	⋯	⋯
2MASS J16220961-1953005	debris/ev. trans.	M3.7	8.90 ± 0.02	138 (−2, +2)	0.07 ± 0.16	2015 May 28	60	⋯	no
2MASS J16230783-2300596	debris/ev. trans.	K3.5	8.18 ± 0.02	139 (−1, +1)	−0.35 ± 0.12	⋯	⋯	⋯	⋯
2MASS J16235385-2946401	debris/ev. trans.	G2.5	7.65 ± 0.02	134 (−1, +1)	0.11 ± 0.12	2015 May 28	40	160	yes
2MASS J16270942-2148457	primordial	M4.5	11.71 ± 0.02	140 (−3, +3)	2.87 ± 0.12	2015 May 27	20	160	no
2MASS J16294879-2137086	primordial	M5	11.52 ± 0.02	131 (−7, +7)	⋯	2013 May 31	60	120	no
2MASS J16303390-2428062	primordial	M4	10.36 ± 0.02	150 (−3, +3)	0.60 ± 0.12	2013 May 30	40	⋯	yes
2MASS J16310240-2408431	primordial	M5	10.79 ± 0.03	136 (−2, +2)	⋯	2013 May 30	60	⋯	no

Notes.
[a] Distances from Bailer-Jones et al. (2018). When no such distance was available, the mean and standard deviation of the rest of the sample, 145 ± 11 pc, were used.
[b] 0.88 mm continuum flux density measured by Barenfeld et al. (2016). Ellipses indicate sources not observed with ALMA.
[c] Ellipses indicate source with previous observation, summarized in Table 2.
[d] Ellipses in only this column indicate sources for which masking observations were not obtained due to the presence of a visual companion seen during observations.
[e] Poor tip-tilt correction as discussed in Section 2.
[f] Target not visible in images as discussed in Section 2.

Table 2
Results from Previous Surveys

Primary	Separation[a] (mas)	ΔK[b] (mag)	K_{comp}[c] (mag)	Position Angle[d] (deg)	Reference
2MASS J15354856-2958551	844 ± 3	0.09 ± 0.08	9.55 ± 0.10	254.40 ± 0.03	Köhler et al. (2000)
2MASS J15583692-2257153	⋯	⋯	⋯	⋯	Kraus et al. (2008)
2MASS J16001330-2418106	⋯	⋯	⋯	⋯	Kraus et al. (2008)
2MASS J16014086-2258103	706 ± 1	0.84 ± 0.03	10.68 ± 0.06	357.5[e]	Bouy et al. (2006)
2MASS J16020039-2221237	⋯	⋯	⋯	⋯	Kraus et al. (2008)
2MASS J16025123-2401574	7198 ± 13	2.91 ± 0.02	11.84 ± 0.06	352.22 ± 0.04	Kraus et al. (2008)
2MASS J16035767-2031055	⋯	⋯	⋯	⋯	Kraus et al. (2008)
2MASS J16042165-2130284	⋯	⋯	⋯	⋯	Kraus et al. (2008)
2MASS J16062196-1928445	578 ± 3	0.64 ± 0.01	9.26 ± 0.06	148.20 ± 0.03	Köhler et al. (2000)
2MASS J16064385-1908056	⋯	⋯	⋯	⋯	Kraus et al. (2008)
2MASS J16070211-2019387	55 ± 2	0.14 ± 0.05	11.54 ± 0.08	271.63 ± 1.08	Kraus & Hillenbrand (2012)
2MASS J16070211-2019387	1483 ± 2	0.85 ± 0.03	12.25 ± 0.07	242.05 ± 0.05	Kraus & Hillenbrand (2012)
2MASS J16082324-1930009	⋯	⋯	⋯	⋯	Kraus et al. (2008)
2MASS J16090075-1908526	⋯	⋯	⋯	⋯	Kraus et al. (2008)
2MASS J16094098-2217594	⋯	⋯	⋯	⋯	Kraus et al. (2008)
2MASS J16095441-1906551	⋯	⋯	⋯	⋯	Kraus et al. (2008)
2MASS J16102174-1904067	4606 ± 2	2.48 ± 0.03	12.10 ± 0.06	6.71 ± 0.03	Kraus et al. (2008)
2MASS J16102857-1904469	299 ± 3	0.42 ± 0.04	9.13 ± 0.07	84.1 ± 0.3	Köhler et al. (2000)
2MASS J16104202-2101319	⋯	⋯	⋯	⋯	Kraus et al. (2008)
2MASS J16111534-1757214	⋯	⋯	⋯	⋯	Kraus et al. (2008)
2MASS J16112057-1820549	⋯	⋯	⋯	⋯	Kraus et al. (2008)
2MASS J16113134-1838259	1310[e]	0.91 ± 0.12	6.72 ± 0.13	213[e]	Eisner et al. (2005)
2MASS J16141107-2305362	222 ± 3	0.21 ± 0.10	7.67 ± 0.12	304.76 ± 0.41	Metchev & Hillenbrand (2009)
2MASS J16142029-1906481	⋯	⋯	⋯	⋯	Lafrenière et al. (2014)
2MASS J16153456-2242421	1907 ± 3	1.19 ± 0.01	9.09 ± 0.05	338.81 ± 0.03	Kraus et al. (2008)
2MASS J16181618-2619080	147 ± 3	0.12 ± 0.03	11.08 ± 0.06	192.3[e]	Bouy et al. (2006)
2MASS J16215466-2043091	⋯	⋯	⋯	⋯	Kraus et al. (2008)
2MASS J16230783-2300596	⋯	⋯	⋯	⋯	Kraus et al. (2008)

Notes.
[a] Ellipses indicate single stars. Contrast limits quoted by the previous studies, shown in Figure 8 and listed in Table 4, are comparable to the current survey.
[b] Difference in K magnitude between primary and companion.
[c] K magnitude of companion.
[d] Position angle is defined east of north.
[e] Uncertainties not provided by authors.

10 or 20 s, respectively. Four targets, 2MASS J16070873-1927341, 2MASS J16071971-2020555, 2MASS J16073939-1917472, and 2MASS J16101473-1919095, were observed on 2011 May 15 as part of a separate program. For these targets, 10 frames of nine seconds each were obtained using the K' filter without a coronagraph in place.

On the observing night of 2015 May 28, tip-tilt errors caused a number of targets to appear blurred in the images. For five of these sources, good quality observations from the previous night were available. For six sources, 2MASS J16020287-2236139, 2MASS J16050231-1941554, 2MASS J16052459-1954419, 2MASS J16064102-2455489, 2MASS J16103956-1916524, and 2MASS J16124893-1800525, there are only data with poor tip-tilt correction. Despite these lower-quality data, we were still able to obtain useful detection limits for these systems in our comparison with other surveys (see Section 4.2). For unknown reasons, 2MASS J16102819-1910444 was not visible in our images during observations. We exclude this source from our sample in the remainder of our analysis.

The NIRC2 Preprocessing and Vortex Image Processing (VIP) packages[10] (Gomez Gonzalez et al. 2017) were used to reduce the imaging observations. This included flat-fielding, dark subtraction, and bad pixel removal, as well as centering

and de-rotation to align and stack individual frames for each target. High-order distortion corrections were applied using the solutions of Yelda et al. (2010) for the 2011 and 2013 data and the updated solutions of Service et al. (2016) for the 2015 data.

2.2. Nonredundant Aperture Masking Observations

Nonredundant aperture masking observations were obtained if no obvious companion was revealed in the initial 10 s images. We used a nine-hole mask with baselines ranging from 1.67 to 8.27 m. Images were read from a 512×512 pixel sub-array of the ALADDIN detector using multiple-correlated double sampling. We obtained six 20 s frames for each target observed in 2013, eight such frames for each target in 2015, and between 40 and 70 frames in 2011. Total integration times are given for each source in Table 1. Depending on the brightness of the target, either 8, 16, or 64 endpoint reads were used along with coadds with shorter integration times in order to avoid saturation.

Reduction of the aperture masking observations followed the procedure described in Kraus et al. (2008; see also Lloyd et al. 2006; Pravdo et al. 2006; Martinache et al. 2007; Kraus et al. 2011).[11] After dark-subtracting and flat-fielding, remaining bad

---

[10] https://github.com/vortex-exoplanet/VIP

[11] Reduction and analysis of the masking data were performed using the Sydney code (https://github.com/mikeireland/idlnrm).

pixels were removed from each frame. Frames were then spatially filtered using a super-Gaussian function of the form $\exp(-kx^4)$ to further reduce read noise. Complex visibilities were extracted from Fourier transforms of the filtered frames. To remove non-common path errors within the telescope and instrument, the data were calibrated using frames of Upper Sco targets that we determined were single. Observations on the night of 2015 May 27 were taken with the telescope in position angle mode rather than vertical angle mode, causing the orientation of the nine-hole mask to change throughout the night and making this calibration more difficult. This led to shallower detection limits for these targets than those observed in vertical angle mode on other nights.

3. Candidate Companion Identification

In this section we present how candidate companions were identified. We first describe the identification of astrophysical sources in our imaging and aperture masking data. We then discuss how the brightnesses and separations of these sources were used to determine whether or not they are likely to be physically associated companions. Finally, we identify potential wide-separation companions using *Gaia*.

3.1. Imaging

Stacked images of each of the 85 Upper Sco targets (excluding 2MASS J16102819-1910444) were searched for potential companions using VIP's *detection* routine. These images were first convolved with the point-spread function (PSF) of the primary star to enhance the signal of any potential companions. A two-dimensional Gaussian was then fit to local maxima of the unsmoothed image to compare the shape of the emission around each maximum to the expected PSF. For fits that displayed positive amplitude, had a center within two pixels of the location of the maximum, and had a full width at half maximum (FWHM) within three pixels of the PSF FWHM, the significance of the detection was determined by measuring its signal-to-noise ratio (S/N) in the unsmoothed image. The S/N was defined as

$$S/N = \frac{F_{\rm source} - F_{\rm bkg}}{\sigma_{\rm bkg}\sqrt{1 + \frac{1}{n}}}, \qquad (1)$$

where $F_{\rm source}$ is the integrated flux of the source within one resolution element equal in diameter to the FWHM of the PSF. $F_{\rm bkg}$ and $\sigma_{\rm bkg}$ are the mean and standard deviation, respectively, of the integrated flux measured in resolution elements around an annulus at the radius of the potential source from the primary star. The number of these resolution elements within the annulus, n, corrects for the small-sample statistics introduced by the low number used (Mawet et al. 2014). Using this technique, we found 170 potential sources with an S/N greater than or equal to five.

Subsequently, each image was inspected by eye to identify any speckles or other artifacts among detected sources that appeared at the same location in images of multiple targets. This inspection also located faint potential sources that the search algorithm missed due to, for example, another bright source or artifact at the same separation from the primary, which would increase the rms noise at that separation. A total of 119 sources were rejected by this inspection, while 10 additional sources were identified.

Principal component analysis (PCA) using VIP was performed to subtract the stellar PSF and speckles from our images and improve our contrast limits (e.g., Amara & Quanz 2012; Soummer et al. 2012). Principal components were constructed from a PSF library composed of frames of other target stars found to be single by the above procedure. PCA was then applied to each target star, with the star itself excluded from the PSF library. We used 13 principal components and a library of 48 reference frames for images taken without the coronagraph. For images taken with the coronagraph, we used seven principal components and a library of 14 reference frames. The above companion detection procedure was then repeated on the PSF-subtracted images.

In all, we identified 61 new sources from direct imaging that appear to be astrophysical but may or may not be physically bound to the primaries. These detections are listed in Table 3. Relative photometry and astrometry of the sources in these systems were measured using the Python package *photutils* (Bradley et al. 2016). The relative positions of primary stars and additional sources were derived from two-dimensional Gaussian fits. For targets with poor AO correction, centroids were estimated using a "center of mass" technique that relied on the moments of a subimage around the source or primary. Uncertainties on positions were estimated by measuring source locations in individual frames for each target and taking the maximum difference between any two frames.

Aperture photometry provided the relative fluxes of the primaries and additional sources with an aperture diameter equal to twice the FWHM of the primary. For systems with a detected source within $0\rlap{.}''3$ of the primary, we used PSF-fitting photometry to measure the positions and relative fluxes. PSFs were constructed with the algorithm described in Kraus et al. (2016), which iteratively uses a library of single-star PSFs to generate template binary PSFs.

We estimated backgrounds and uncertainties in our aperture photometry using the mean and standard deviation of 20 apertures around an annulus at the same distance from the target source as the newly detected source. This accounts for both read noise and speckle noise, as well as any light from the primary that is included in our aperture photometry, as any such contamination will be incorporated into our background subtraction and uncertainties. To measure background and uncertainties in the photometry of the primary stars, apertures were randomly positioned in annuli between $2''$ and $2\rlap{.}''5$ from the primary. For 2MASS J15562477-2225552, 2MASS J16020287-2236139, 2MASS J16020757-2257467, 2MASS J16041740-1942287, 2MASS J16054540-2023088, 2MASS J16093558-1828232, and 2MASS J16220961-1953005, where sources lie within this separation range, annuli from $3\rlap{.}''5$ to $4''$ were used.

For our detected sources, photometric calibrations used the 2MASS K_s magnitude of the primary and the ratio of integrated counts between each source and primary. For systems with a source located within the $2\rlap{.}''6$ FWHM of the 2MASS PSF (Skrutskie et al. 2006), we separated out the K_s magnitude attributable only to the primary. In addition to the photometric uncertainties described above, the uncertainties in new source magnitudes include the statistical uncertainty in the 2MASS magnitude of the primary and an assumed uncertainty of 0.05 magnitudes due to K-band variability of the primary (Carpenter et al. 2001). Since the primary star is saturated in our images of 2MASS J16041740-1942287, 2MASS J16101888-2502325,

Table 3
Newly Detected Sources

Primary Star	Detection Technique	Separation (mas)	ΔK[a] (mag)	K_{comp}[a] (mag)	Position Angle[a] (deg)	Candidate Companion?[b]
2MASS J15530132-2114135	Imaging	1690.2 ± 11.4	7.13 ± 0.10	18.15 ± 0.11	249.50 ± 0.39	no
2MASS J15534211-2049282	Imaging	321.8 ± 0.1	1.47 ± 0.01	11.55 ± 0.06	254.59 ± 0.02	yes
2MASS J15534211-2049282	Imaging	1097.1 ± 0.1	1.47 ± 0.01	11.55 ± 0.06	68.44 ± 0.01	yes
2MASS J15554883-2512240	Imaging	2306.2 ± 0.8	5.87 ± 0.01	14.17 ± 0.06	353.85 ± 0.02	no
2MASS J15562477-2225552	Imaging	2129.8 ± 18.9	7.79 ± 0.17	18.58 ± 0.18	59.77 ± 0.51	no
2MASS J15570641-2206060	Imaging	4381.7 ± 39.1	6.90 ± 0.08	18.19 ± 0.10	181.63 ± 0.51	no
2MASS J15572986-2258438	Imaging	194.4 ± 1.5	0.26 ± 0.06	12.04 ± 0.08	145.32 ± 0.44	yes
2MASS J16001730-2236504	Masking	43.1 ± 1.4	1.70 ± 0.06	11.64 ± 0.08	290.74 ± 1.22	yes
2MASS J16001730-2236504	Imaging	5347.8 ± 0.2	8.43 ± 0.05	18.37 ± 0.07	140.83 ± 0.01	no
2MASS J16001730-2236504	Imaging	4209.9 ± 0.7	8.73 ± 0.06	18.67 ± 0.08	186.04 ± 0.01	no
2MASS J16001844-2230114	Imaging	142.5 ± 1.5	0.88 ± 0.04	11.68 ± 0.07	251.25 ± 0.60	yes
2MASS J16001844-2230114	Imaging	6173.4 ± 0.4	7.19 ± 0.03	17.99 ± 0.06	317.23 ± 0.01	no
2MASS J16014157-2111380	Imaging	2435.5 ± 29.7	6.70 ± 0.21	18.38 ± 0.22	334.91 ± 0.70	no
2MASS J16020287-2236139	Imaging	2438.1 ± 2.7	0.90 ± 0.01	12.91 ± 0.06	94.21 ± 0.06	no
2MASS J16020757-2257467	Imaging	3280.4 ± 0.5	6.57 ± 0.01	16.43 ± 0.06	343.01 ± 0.01	no
2MASS J16020757-2257467	Imaging	2483.0 ± 0.9	7.45 ± 0.02	17.31 ± 0.06	163.85 ± 0.02	no
2MASS J16030161-2207523	Imaging	5378.5 ± 0.6	4.61 ± 0.02	16.34 ± 0.06	49.60 ± 0.01	no
2MASS J16032225-2413111	Imaging	5048.7 ± 0.6	6.21 ± 0.01	16.22 ± 0.05	58.11 ± 0.01	no
2MASS J16032225-2413111	Imaging	3145.3 ± 7.2	10.12 ± 0.25	20.13 ± 0.26	231.83 ± 0.13	no
2MASS J16033471-1829303	Imaging	62.7 ± 1.6	0.08 ± 0.05	12.11 ± 0.08	158.64 ± 1.35	yes
2MASS J16035793-1942108	Imaging	6034.5 ± 16.3	9.17 ± 0.16	19.49 ± 0.17	251.75 ± 0.15	no
2MASS J16041740-1942287	Imaging	4978.9 ± 17.2	1.03 ± 0.24	11.45 ± 0.23	353.22 ± 0.20	no
2MASS J16041740-1942287	Imaging	2158.9 ± 3.1	8.42 ± 0.27	18.84 ± 0.26	114.32 ± 0.08	no
2MASS J16043916-1942459	Masking	25.4 ± 0.4	0.15 ± 0.04	10.94 ± 0.07	42.10 ± 1.40	yes
2MASS J16052556-2035397	Imaging	534.9 ± 1.6	0.97 ± 0.01	12.63 ± 0.06	350.02 ± 0.16	yes
2MASS J16052556-2035397	Imaging	94.5 ± 1.9	1.13 ± 0.02	12.80 ± 0.06	81.65 ± 1.77	yes
2MASS J16052661-1957050	Imaging	356.6 ± 0.3	0.19 ± 0.01	11.54 ± 0.06	88.77 ± 0.05	yes
2MASS J16054540-2023088	Imaging	2038.9 ± 1.0	3.03 ± 0.01	13.51 ± 0.06	48.24 ± 0.03	no
2MASS J16054540-2023088	Imaging	1529.2 ± 1.9	7.05 ± 0.09	17.53 ± 0.10	143.01 ± 0.07	no
2MASS J16060061-1957114	Imaging	1079.9 ± 0.4	0.05 ± 0.01	11.22 ± 0.06	139.76 ± 0.02	yes
2MASS J16062277-2011243	Imaging	5712.0 ± 51.8	5.74 ± 0.02	16.74 ± 0.06	7.54 ± 0.52	no
2MASS J16063539-2516510	Imaging	4995.5 ± 6.3	5.95 ± 0.04	17.66 ± 0.07	152.29 ± 0.07	no
2MASS J16070014-2033092	Imaging	3055.1 ± 1.7	8.15 ± 0.03	18.09 ± 0.06	28.96 ± 0.03	no
2MASS J16070873-1927341	Masking	19.3 ± 0.7	0.27 ± 0.10	11.44 ± 0.11	289.13 ± 2.73	yes
2MASS J16072747-2059442	Imaging	566.6 ± 1.2	0.12 ± 0.01	11.03 ± 0.05	112.56 ± 0.12	yes
2MASS J16075796-2040087	Masking	31.9 ± 3.7	2.14 ± 0.24	9.95 ± 0.25	357.53 ± 2.65	yes
2MASS J16080555-2218070	Masking	25.5 ± 1.3	1.20 ± 0.20	11.05 ± 0.21	24.40 ± 2.20	yes
2MASS J16080555-2218070	Imaging	4770.1 ± 1.5	6.33 ± 0.01	16.19 ± 0.05	291.05 ± 0.02	no
2MASS J16082733-2217292	Imaging	3119.5 ± 2.5	7.28 ± 0.02	17.86 ± 0.06	315.01 ± 0.05	no
2MASS J16082751-1949047	Imaging	183.0 ± 1.6	0.02 ± 0.01	11.36 ± 0.05	20.25 ± 0.47	yes
2MASS J16082870-2137198	Imaging	2665.3 ± 22.8	8.27 ± 0.21	19.03 ± 0.22	350.28 ± 0.49	no
2MASS J16093558-1828232	Imaging	2130.7 ± 6.4	8.08 ± 0.10	18.78 ± 0.11	81.59 ± 0.17	no
2MASS J16095361-1754474	Imaging	4321.0 ± 53.2	7.99 ± 0.22	19.52 ± 0.22	156.51 ± 0.70	no
2MASS J16095933-1800090	Imaging	3691.8 ± 0.2	7.44 ± 0.02	17.78 ± 0.06	150.03 ± 0.01	no
2MASS J16101888-2502325	Imaging	4896.5 ± 2.0	0.11 ± 0.13	11.38 ± 0.11	241.10 ± 0.02	no
2MASS J16103956-1916524	Imaging	1026.7 ± 0.6	5.42 ± 0.14	15.69 ± 0.15	168.04 ± 0.03	no
2MASS J16111330-2019029	Imaging	3790.7 ± 0.8	7.52 ± 0.01	17.07 ± 0.06	4.38 ± 0.01	no
2MASS J16115091-2012098	Imaging	1094.2 ± 0.1	5.67 ± 0.01	16.07 ± 0.06	230.79 ± 0.01	no
2MASS J16115091-2012098	Imaging	2112.6 ± 1.7	9.05 ± 0.14	19.45 ± 0.15	169.89 ± 0.05	no
2MASS J16122737-2009596	Imaging	4285.3 ± 0.3	3.25 ± 0.01	14.78 ± 0.06	9.98 ± 0.01	no
2MASS J16124893-1800525	Imaging	3161.9 ± 2.2	2.99 ± 0.02	13.35 ± 0.06	10.82 ± 0.04	no
2MASS J16133650-2503473	Imaging	138.4 ± 1.8	0.26 ± 0.01	11.14 ± 0.05	29.53 ± 0.66	yes
2MASS J16135434-2320342	Imaging	617.7 ± 0.1	0.54 ± 0.01	11.11 ± 0.06	108.26 ± 0.01	yes
2MASS J16142893-1857224	Masking	37.0 ± 1.3	1.69 ± 0.06	11.16 ± 0.08	256.50 ± 1.20	yes
2MASS J16145918-2750230	Imaging	3803.2 ± 2.1	9.73 ± 0.06	18.41 ± 0.08	151.08 ± 0.03	no
2MASS J16145928-2459308	Imaging	4283.6 ± 19.8	5.91 ± 0.02	16.99 ± 0.06	16.20 ± 0.50	no
2MASS J16145928-2459308	Imaging	4682.2 ± 40.9	7.39 ± 0.07	18.48 ± 0.09	151.41 ± 0.26	no
2MASS J16154416-1921171	Imaging	2993.7 ± 0.7	9.98 ± 0.16	18.38 ± 0.15	176.20 ± 0.01	no
2MASS J16220961-1953005	Imaging	1790.9 ± 0.8	2.90 ± 0.01	11.87 ± 0.06	225.30 ± 0.12	yes
2MASS J16220961-1953005	Imaging	2880.5 ± 0.1	4.48 ± 0.01	13.45 ± 0.06	359.90 ± 0.01	no
2MASS J16220961-1953005	Imaging	1572.4 ± 3.2	7.28 ± 0.14	16.25 ± 0.15	112.99 ± 0.03	no
2MASS J16235385-2946401	Imaging	5890.3 ± 5.5	7.07 ± 0.34	14.73 ± 0.34	9.68 ± 0.05	no

Table 3
(Continued)

Primary Star	Detection Technique	Separation (mas)	ΔK^a (mag)	K_{comp}^a (mag)	Position Angle[a] (deg)	Candidate Companion?[b]
2MASS J16235385-2946401	Imaging	4888.5 ± 11.9	7.13 ± 0.37	14.78 ± 0.38	13.83 ± 0.14	no
2MASS J16303390-2428062	Imaging	3409.2 ± 0.4	7.00 ± 0.03	17.36 ± 0.06	234.41 ± 0.01	no
2MASS J16303390-2428062	Imaging	4290.7 ± 4.4	7.47 ± 0.05	17.83 ± 0.08	146.75 ± 0.06	no
2MASS J16303390-2428062	Imaging	5177.7 ± 1.6	8.53 ± 0.16	18.89 ± 0.17	120.86 ± 0.02	no
2MASS J16310240-2408431	Imaging	3347.8 ± 11.0	6.45 ± 0.05	17.24 ± 0.08	318.22 ± 0.19	no

Notes.
[a] ΔK, K_{comp}, and position angle are defined as in Table 2.
[b] Sources are considered to be candidate companions if they satisfy $K_{comp} < 15$ and separation $< 2''$.

and 2MASS J16154416-1921171, the K magnitudes of the additional sources in these systems were determined using other targets observed during the same two-night runs to convert counts to K magnitude. The separations and magnitudes of our newly detected sources are listed in Table 3.

Contrast limits are calculated for single stars using VIP's *contrast curve* routine. This routine injects fake companions with a range of separations and contrasts relative to the primary into the stacked, PSF-subtracted frames for each target. The 5σ contrast limit is measured as the contrast of the brightest companion that is recovered with an S/N of less than five. As above, noise is measured in the annulus at the angular separation of the fake companion using Equation (1). Our imaging contrast limits for sources without candidate companions (see Section 3.3) are listed in Table 4.

3.2. Nonredundant Aperture Masking

Nonredundant aperture masking achieves deeper contrast limits than traditional AO imaging at separations within a few hundred milliarcseconds using closure phases. At these separations, imaging contrast is limited by speckle noise created by atmospheric turbulence. This same turbulence introduces errors in the relative phases of the light reaching pairs of holes in the aperture mask. However, if these relative phases are summed around a triangle of the baselines connecting each pair, phase errors specific to individual holes, such as those due to atmospheric effects, will cancel out (e.g., Lohmann et al. 1983; Readhead et al. 1988). The resulting closure phases can then be used to search for close companions.

To locate companions in the aperture masking data, we adopted the technique used by Kraus et al. (2008). Briefly, χ^2 minimization was used to find the best-fit separation, contrast, and position angle of a potential companion for the closure phases of each target, along with the uncertainties in each of these parameters. The detection sensitivity to companions as a function of separation from the primary star was determined using 10,000 simulated data sets of a single star observed with the same (u, v)-sampling and closure phase errors as the observed data. The same fitting procedure was used to find the brightest detected companion in different annuli in each simulated data set. The detection threshold for each annulus was defined as the contrast ratio above which no potential companions were detected in 99.9% of the simulated data sets. Table 3 lists the six companions identified above this threshold. Table 4 provides the contrast limits of the remaining targets.

3.3. Selection of Candidate Companions

The sources we detected are not necessarily bound companions to the host star. With only a single epoch of observations, we cannot use common proper motion to rule out the chance alignment of a field star. Instead, we use the brightness and separation of sources to distinguish between field stars and candidate companions. Figure 1 shows the K magnitudes and separations of the 67 sources found by imaging and masking and the 12 literature companions listed in Table 2. We used the TRILEGAL galactic population models (Girardi et al. 2005) to simulate the population of field stars as a function of K magnitude in the direction of Upper Sco. We find a density of 2.2×10^{-4} field objects per square arcsecond brighter than $K = 15$. For our full sample of 112 targets, we would expect a total of less than one such field star to be within $2''$ of a target star by chance. We therefore consider any sources brighter than $K = 15$ and within $2''$ of a target star likely to be a candidate bound companion. These limits are the same as those used in Kraus et al. (2008) to identify candidate companions in Upper Sco and are shown in Figure 1 as dashed lines. Sources that meet these criteria are indicated in the "Candidate Companion" column of Table 3. For consistency, we apply these criteria to the previously known companions in Table 2, even if objects beyond these limits have been confirmed to be associated by other methods.

Figure 2 presents the color–magnitude diagram for sources in the *Gaia* DR2 Catalog (Gaia Collaboration et al. 2016, 2018). The candidate companions that meet our criteria for physical association lie along the same sequence as the primary stars, as would be expected for co-evolutionary companions at the same distance from Earth. The sources that do not meet these criteria include a small number of objects that match the colors and magnitudes of the candidate companions and primaries. However, the majority of objects outside of our selection criteria are fainter and bluer than the primary star sequence, as would be expected for background field stars. While we cannot rule out that a fraction of sources fainter than $K = 15$ and separated by more than $2''$ are physically associated companions, there is a significant fraction of field objects beyond these limits.

We note that the sources beyond $2''$ that are fainter than $K \sim 12.5$–13 would be candidate brown dwarfs ($M \lesssim 0.08\, M_\odot$) if they were associated, assuming a distance and age of 145 pc and 5–10 Myr (Chabrier et al. 2000; Baraffe et al. 2002). Similarly, sources fainter than $K \sim 15.5$–16 would be potential giant planets ($M \lesssim 13\, M_{Jup}$) if they were bound. While these objects are most likely field stars, they may be worth observing in the future to look for common proper motion.

Table 4
Contrast Limits for Systems without Detected Companions

Primary	Technique	ΔK [a]								
		10–20	20–40	40–80	80–160	160–240	240–320	320–500	500–1000	>1000
2MASS J15514032-2146103	Imaging	⋯	⋯	1.72	3.39	4.64	7.48	6.97	8.12	8.41
2MASS J15514032-2146103	Coronagraph	⋯	⋯	⋯	⋯	⋯	⋯	⋯	⋯	⋯
2MASS J15514032-2146103	Masking	0.00	2.34	3.56	3.22	2.55	1.13	⋯	⋯	⋯
2MASS J15521088-2125372	Imaging	⋯	⋯	⋯	0.75	2.24	4.27	4.39	5.98	6.45
2MASS J15521088-2125372	Coronagraph	⋯	⋯	⋯	⋯	⋯	⋯	⋯	⋯	⋯
2MASS J15521088-2125372	Masking	0.00	0.00	0.00	0.00	0.00	0.00	⋯	⋯	⋯
2MASS J15530132-2114135	Imaging	⋯	⋯	0.81	3.27	4.45	7.33	6.88	7.78	8.26
2MASS J15530132-2114135	Coronagraph	⋯	⋯	⋯	⋯	⋯	⋯	⋯	⋯	⋯
2MASS J15530132-2114135	Masking	0.00	1.42	2.84	2.45	1.75	0.31	⋯	⋯	⋯
2MASS J15551704-2322165	Imaging	⋯	⋯	1.50	2.96	3.92	5.01	5.93	7.77	8.15
2MASS J15551704-2322165	Coronagraph	⋯	⋯	⋯	⋯	⋯	⋯	7.25	8.86	11.34
2MASS J15551704-2322165	Masking	0.00	0.00	0.33	0.10	0.00	0.00	⋯	⋯	⋯
2MASS J15554883-2512240	Imaging	⋯	⋯	2.66	3.63	4.42	5.86	6.29	7.03	7.21
2MASS J15554883-2512240	Coronagraph	⋯	⋯	⋯	⋯	⋯	⋯	4.62	5.95	9.02
2MASS J15554883-2512240	Masking	0.00	2.83	3.91	3.60	3.04	1.79	⋯	⋯	⋯
2MASS J15562477-2225552	Imaging	⋯	⋯	1.57	3.23	4.47	7.77	7.10	8.09	8.39
2MASS J15562477-2225552	Coronagraph	⋯	⋯	⋯	⋯	⋯	⋯	⋯	⋯	⋯
2MASS J15562477-2225552	Masking	0.00	1.76	3.10	2.73	2.03	0.54	⋯	⋯	⋯
2MASS J15570641-2206060	Imaging	⋯	⋯	1.35	2.99	4.34	3.20	7.28	8.43	8.70
2MASS J15570641-2206060	Coronagraph	⋯	⋯	⋯	⋯	⋯	⋯	⋯	⋯	⋯
2MASS J15570641-2206060	Masking	0.55	3.61	4.66	4.42	3.79	2.72	⋯	⋯	⋯
2MASS J15581270-2328364	Imaging	⋯	⋯	2.50	3.48	4.34	6.38	6.34	7.59	8.02
2MASS J15581270-2328364	Coronagraph	⋯	⋯	⋯	⋯	⋯	⋯	0.65	5.59	9.39
2MASS J15581270-2328364	Masking	3.12	4.93	5.77	5.67	5.42	5.02	⋯	⋯	⋯
2MASS J15582981-2310077	Imaging	⋯	⋯	1.64	3.21	4.33	5.48	6.89	8.04	8.41
2MASS J15582981-2310077	Coronagraph	⋯	⋯	⋯	⋯	⋯	⋯	6.75	7.52	7.89
2MASS J15582981-2310077	Masking	0.00	1.51	2.91	2.53	1.84	0.40	⋯	⋯	⋯
2MASS J15583692-2257153	Imaging	⋯	⋯	⋯	⋯	⋯	⋯	4.00	5.00	10.00
2MASS J15583692-2257153	Coronagraph	⋯	⋯	⋯	⋯	⋯	⋯	⋯	⋯	⋯
2MASS J15583692-2257153	Masking	⋯	3.49	5.06	5.43	5.35	⋯	⋯	⋯	⋯
2MASS J15584772-1757595	Imaging	⋯	⋯	2.27	3.26	4.15	5.59	6.58	7.07	7.31
2MASS J15584772-1757595	Coronagraph	⋯	⋯	⋯	⋯	⋯	⋯	1.20	5.69	9.38
2MASS J15584772-1757595	Masking	⋯	3.12	4.71	5.03	4.97	⋯	⋯	⋯	⋯
2MASS J16001330-2418106	Imaging	⋯	⋯	⋯	⋯	⋯	⋯	4.00	5.00	7.00
2MASS J16001330-2418106	Coronagraph	⋯	⋯	⋯	⋯	⋯	⋯	⋯	⋯	⋯
2MASS J16001330-2418106	Masking	2.72	4.55	5.27	5.18	4.80	4.26	⋯	⋯	⋯
2MASS J16014157-2111380	Imaging	⋯	⋯	⋯	0.14	1.31	2.92	4.32	6.03	6.71
2MASS J16014157-2111380	Coronagraph	⋯	⋯	⋯	⋯	⋯	⋯	⋯	⋯	⋯
2MASS J16014157-2111380	Masking	0.00	2.61	3.65	3.45	2.73	1.29	⋯	⋯	⋯
2MASS J16020039-2221237	Imaging	⋯	⋯	⋯	⋯	⋯	⋯	4.00	5.00	8.00
2MASS J16020039-2221237	Coronagraph	⋯	⋯	⋯	⋯	⋯	⋯	⋯	⋯	⋯
2MASS J16020039-2221237	Masking	0.45	3.46	4.46	4.32	4.21	4.10	⋯	⋯	⋯
2MASS J16020287-2236139	Imaging	⋯	⋯	⋯	⋯	⋯	0.00	0.82	2.50	3.58
2MASS J16020287-2236139	Coronagraph	⋯	⋯	⋯	⋯	⋯	⋯	⋯	⋯	⋯
2MASS J16020287-2236139	Masking	⋯	⋯	⋯	⋯	⋯	⋯	⋯	⋯	⋯
2MASS J16020757-2257467	Imaging	⋯	⋯	1.87	3.67	4.92	7.62	7.46	7.76	7.97
2MASS J16020757-2257467	Coronagraph	⋯	⋯	⋯	⋯	⋯	⋯	7.81	8.52	10.47
2MASS J16020757-2257467	Masking	0.79	3.83	4.77	4.49	3.93	2.79	⋯	⋯	⋯
2MASS J16024152-2138245	Imaging	⋯	⋯	⋯	0.36	1.82	2.91	5.30	6.96	7.53
2MASS J16024152-2138245	Coronagraph	⋯	⋯	⋯	⋯	⋯	⋯	⋯	⋯	⋯
2MASS J16024152-2138245	Masking	0.00	2.19	3.43	3.22	2.48	0.79	⋯	⋯	⋯
2MASS J16025123-2401574	Imaging	⋯	⋯	1.57	3.08	4.25	6.13	6.39	7.79	8.33
2MASS J16025123-2401574	Coronagraph	⋯	⋯	⋯	⋯	⋯	⋯	7.70	8.97	11.72
2MASS J16025123-2401574	Masking	⋯	2.52	4.08	4.58	4.50	⋯	⋯	⋯	⋯
2MASS J16030161-2207523	Imaging	⋯	⋯	0.70	2.38	3.56	5.75	5.58	7.51	8.03
2MASS J16030161-2207523	Coronagraph	⋯	⋯	⋯	⋯	⋯	⋯	⋯	⋯	⋯
2MASS J16030161-2207523	Masking	0.00	0.58	2.10	1.61	0.63	0.00	⋯	⋯	⋯
2MASS J16031329-2112569	Imaging	⋯	⋯	1.34	2.84	4.02	5.99	5.98	7.57	8.29
2MASS J16031329-2112569	Coronagraph	⋯	⋯	⋯	⋯	⋯	⋯	⋯	⋯	⋯
2MASS J16031329-2112569	Masking	0.00	0.58	2.09	1.60	0.63	0.00	⋯	⋯	⋯
2MASS J16032225-2413111	Imaging	⋯	⋯	1.72	3.32	4.30	4.59	6.88	8.08	8.12
2MASS J16032225-2413111	Coronagraph	⋯	⋯	⋯	⋯	⋯	⋯	7.17	8.52	10.47

Table 4
(Continued)

Primary	Technique	ΔK^{a}								
		10–20	20–40	40–80	80–160	160–240	240–320	320–500	500–1000	>1000
2MASS J16032225-2413111	Masking	0.40	3.42	4.40	4.17	3.59	2.41	⋯	⋯	⋯
2MASS J16035767-2031055	Imaging	⋯	⋯	⋯	⋯	⋯	⋯	4.00	5.00	9.00
2MASS J16035767-2031055	Coronagraph	⋯	⋯	⋯	⋯	⋯	⋯	⋯	⋯	⋯
2MASS J16035767-2031055	Masking	⋯	2.86	4.45	4.94	4.86	⋯	⋯	⋯	⋯
2MASS J16035793-1942108	Imaging	⋯	⋯	1.69	3.16	4.03	4.00	6.28	6.55	6.65
2MASS J16035793-1942108	Coronagraph	⋯	⋯	⋯	⋯	⋯	⋯	6.91	8.48	10.19
2MASS J16035793-1942108	Masking	0.05	2.99	4.07	3.76	3.18	1.92	⋯	⋯	⋯
2MASS J16041740-1942287	Imaging	⋯	⋯	⋯	0.90	2.41	4.37	5.65	7.63	7.77
2MASS J16041740-1942287	Coronagraph	⋯	⋯	⋯	⋯	⋯	⋯	⋯	⋯	⋯
2MASS J16041740-1942287	Masking	⋯	⋯	⋯	⋯	⋯	⋯	⋯	⋯	⋯
2MASS J16042165-2130284	Imaging	⋯	⋯	⋯	⋯	⋯	⋯	4.00	5.00	8.00
2MASS J16042165-2130284	Coronagraph	⋯	⋯	⋯	⋯	⋯	⋯	⋯	⋯	⋯
2MASS J16042165-2130284	Masking	3.57	5.43	6.23	6.15	5.79	5.50	⋯	⋯	⋯
2MASS J16050231-1941554	Imaging	⋯	⋯	⋯	⋯	0.01	0.45	2.67	3.66	5.05
2MASS J16050231-1941554	Coronagraph	⋯	⋯	⋯	⋯	⋯	⋯	⋯	⋯	⋯
2MASS J16050231-1941554	Masking	⋯	⋯	⋯	⋯	⋯	⋯	⋯	⋯	⋯
2MASS J16052459-1954419	Imaging	⋯	⋯	⋯	⋯	⋯	0.00	1.67	3.41	5.18
2MASS J16052459-1954419	Coronagraph	⋯	⋯	⋯	⋯	⋯	⋯	⋯	⋯	⋯
2MASS J16052459-1954419	Masking	⋯	⋯	⋯	⋯	⋯	⋯	⋯	⋯	⋯
2MASS J16053215-1933159	Imaging	⋯	⋯	1.52	2.95	3.87	5.26	6.93	8.11	8.59
2MASS J16053215-1933159	Coronagraph	⋯	⋯	⋯	⋯	⋯	⋯	⋯	⋯	⋯
2MASS J16053215-1933159	Masking	0.04	2.99	4.07	3.76	3.17	1.95	⋯	⋯	⋯
2MASS J16054540-2023088	Imaging	⋯	⋯	0.54	2.11	3.35	5.04	5.90	7.33	7.88
2MASS J16054540-2023088	Coronagraph	⋯	⋯	⋯	⋯	⋯	⋯	⋯	⋯	⋯
2MASS J16054540-2023088	Masking	⋯	⋯	⋯	⋯	⋯	⋯	⋯	⋯	⋯
2MASS J16055863-1949029	Imaging	⋯	⋯	⋯	0.98	2.52	4.47	5.33	6.91	7.41
2MASS J16055863-1949029	Coronagraph	⋯	⋯	⋯	⋯	⋯	⋯	5.52	7.29	8.84
2MASS J16055863-1949029	Masking	0.00	1.12	2.66	2.32	1.55	0.13	⋯	⋯	⋯
2MASS J16061144-1935405	Imaging	⋯	⋯	0.62	2.27	3.55	6.04	6.58	7.72	7.91
2MASS J16061144-1935405	Coronagraph	⋯	⋯	⋯	⋯	⋯	⋯	⋯	⋯	⋯
2MASS J16061144-1935405	Masking	0.00	2.92	4.06	3.73	3.15	1.83	⋯	⋯	⋯
2MASS J16061330-2212537	Imaging	⋯	⋯	0.83	2.70	4.23	6.37	6.08	7.87	8.22
2MASS J16061330-2212537	Coronagraph	⋯	⋯	⋯	⋯	⋯	⋯	7.51	9.41	10.81
2MASS J16061330-2212537	Masking	⋯	⋯	⋯	⋯	⋯	⋯	⋯	⋯	⋯
2MASS J16062277-2011243	Imaging	⋯	⋯	1.62	3.20	4.47	6.52	7.41	8.42	8.39
2MASS J16062277-2011243	Coronagraph	⋯	⋯	⋯	⋯	⋯	⋯	⋯	⋯	⋯
2MASS J16062277-2011243	Masking	1.15	4.01	5.12	4.87	4.29	3.24	⋯	⋯	⋯
2MASS J16063539-2516510	Imaging	⋯	⋯	0.61	2.19	3.4	6.13	7.02	7.53	7.87
2MASS J16063539-2516510	Coronagraph	⋯	⋯	⋯	⋯	⋯	⋯	⋯	⋯	⋯
2MASS J16063539-2516510	Masking	0.00	2.27	3.46	3.13	2.49	1.02	⋯	⋯	⋯
2MASS J16064102-2455489	Imaging	⋯	⋯	⋯	⋯	0.05	0.81	2.90	4.00	5.13
2MASS J16064102-2455489	Coronagraph	⋯	⋯	⋯	⋯	⋯	⋯	⋯	⋯	⋯
2MASS J16064102-2455489	Masking	0.00	0.39	1.75	1.35	0.47	0.00	⋯	⋯	⋯
2MASS J16064115-2517044	Imaging	⋯	⋯	2.03	3.63	4.86	6.87	7.10	8.25	8.57
2MASS J16064115-2517044	Coronagraph	⋯	⋯	⋯	⋯	⋯	⋯	⋯	⋯	⋯
2MASS J16064115-2517044	Masking	0.00	2.56	3.65	3.42	2.76	1.26	⋯	⋯	⋯
2MASS J16064385-1908056	Imaging	⋯	⋯	⋯	⋯	⋯	⋯	4.00	5.00	8.00
2MASS J16064385-1908056	Coronagraph	⋯	⋯	⋯	⋯	⋯	⋯	⋯	⋯	⋯
2MASS J16064385-1908056	Masking	⋯	⋯	⋯	⋯	⋯	⋯	⋯	⋯	⋯
2MASS J16070014-2033092	Imaging	⋯	⋯	2.03	3.83	5.46	9.66	7.66	7.72	7.87
2MASS J16070014-2033092	Coronagraph	⋯	⋯	⋯	⋯	⋯	⋯	7.53	8.75	10.81
2MASS J16070014-2033092	Masking	2.28	4.75	5.70	5.50	4.90	3.78	⋯	⋯	⋯
2MASS J16071971-2020555	Imaging	⋯	⋯	0.00	0.69	2.37	1.40	4.96	6.46	6.80
2MASS J16071971-2020555	Coronagraph	⋯	⋯	⋯	⋯	⋯	⋯	⋯	⋯	⋯
2MASS J16071971-2020555	Masking	0.00	1.71	3.18	2.89	2.24	0.58	⋯	⋯	⋯
2MASS J16072625-2432079	Imaging	⋯	⋯	1.70	3.14	4.1	6.51	6.89	7.44	7.53
2MASS J16072625-2432079	Coronagraph	⋯	⋯	⋯	⋯	⋯	⋯	6.93	8.36	10.47
2MASS J16072625-2432079	Masking	0.18	3.17	4.18	3.91	3.29	2.07	⋯	⋯	⋯
2MASS J16073939-1917472	Imaging	⋯	⋯	0.18	1.64	3.14	1.79	5.72	7.49	8.50
2MASS J16073939-1917472	Coronagraph	⋯	⋯	⋯	⋯	⋯	⋯	⋯	⋯	⋯
2MASS J16073939-1917472	Masking	0.93	3.87	4.90	4.66	4.58	4.37	⋯	⋯	⋯
2MASS J16081566-2222199	Imaging	⋯	⋯	2.47	4.33	5.36	6.58	7.80	8.28	8.52

Table 4
(Continued)

Primary	Technique	ΔK[a]								
		10–20	20–40	40–80	80–160	160–240	240–320	320–500	500–1000	>1000
2MASS J16081566-2222199	Coronagraph	⋯	⋯	⋯	⋯	⋯	⋯	7.77	8.58	10.70
2MASS J16081566-2222199	Masking	0.48	3.53	4.46	4.22	3.59	2.46	⋯	⋯	⋯
2MASS J16082324-1930009	Imaging	⋯	⋯	⋯	⋯	⋯	⋯	4.00	5.00	8.00
2MASS J16082324-1930009	Coronagraph	⋯	⋯	⋯	⋯	⋯	⋯	⋯	⋯	⋯
2MASS J16082324-1930009	Masking	3.79	5.64	6.46	6.35	6.20	5.77	⋯	⋯	⋯
2MASS J16082733-2217292	Imaging	⋯	⋯	0.03	0.40	0.65	1.06	0.85	6.30	7.15
2MASS J16082733-2217292	Coronagraph	⋯	⋯	⋯	⋯	⋯	⋯	7.20	8.83	10.10
2MASS J16082733-2217292	Masking	⋯	⋯	1.90	3.57	4.99	3.32	7.49	7.97	7.98
2MASS J16082870-2137198	Imaging	⋯	⋯	1.13	3.14	5.23	7.08	7.44	8.43	8.82
2MASS J16082870-2137198	Coronagraph	⋯	⋯	⋯	⋯	⋯	⋯	⋯	⋯	⋯
2MASS J16082870-2137198	Masking	0.00	2.99	4.34	4.08	3.42	2.24	⋯	⋯	⋯
2MASS J16083455-2211559	Imaging	⋯	⋯	⋯	⋯	0.02	0.85	2.99	5.38	6.47
2MASS J16083455-2211559	Coronagraph	⋯	⋯	⋯	⋯	⋯	⋯	⋯	⋯	⋯
2MASS J16083455-2211559	Masking	0.00	2.19	3.65	3.38	2.71	1.21	⋯	⋯	⋯
2MASS J16084894-2400045	Imaging	⋯	⋯	2.12	3.69	4.77	6.77	7.16	8.31	8.52
2MASS J16084894-2400045	Coronagraph	⋯	⋯	⋯	⋯	⋯	⋯	⋯	⋯	⋯
2MASS J16084894-2400045	Masking	0.64	3.71	4.80	4.53	3.97	2.85	⋯	⋯	⋯
2MASS J16090002-1908368	Imaging	⋯	⋯	1.91	3.57	4.85	6.72	7.13	8.49	8.67
2MASS J16090002-1908368	Coronagraph	⋯	⋯	⋯	⋯	⋯	⋯	⋯	⋯	⋯
2MASS J16090002-1908368	Masking	0.14	3.12	4.15	3.83	3.25	2.08	⋯	⋯	⋯
2MASS J16090075-1908526	Imaging	⋯	⋯	⋯	⋯	⋯	⋯	4.00	5.00	8.00
2MASS J16090075-1908526	Coronagraph	⋯	⋯	⋯	⋯	⋯	⋯	⋯	⋯	⋯
2MASS J16090075-1908526	Masking	3.81	5.63	6.38	6.33	6.14	5.72	⋯	⋯	⋯
2MASS J16093558-1828232	Imaging	⋯	⋯	0.99	2.82	4.57	3.48	7.14	8.29	8.83
2MASS J16093558-1828232	Coronagraph	⋯	⋯	⋯	⋯	⋯	⋯	⋯	⋯	⋯
2MASS J16093558-1828232	Masking	0.17	3.16	4.13	3.78	3.19	2.00	⋯	⋯	⋯
2MASS J16094098-2217594	Imaging	⋯	⋯	⋯	⋯	⋯	⋯	4.00	5.00	9.00
2MASS J16094098-2217594	Coronagraph	⋯	⋯	⋯	⋯	⋯	⋯	⋯	⋯	⋯
2MASS J16094098-2217594	Masking	⋯	2.34	3.93	4.43	4.30	⋯	⋯	⋯	⋯
2MASS J16095361-1754474	Imaging	⋯	⋯	1.69	3.28	4.65	6.86	7.07	8.06	8.18
2MASS J16095361-1754474	Coronagraph	⋯	⋯	⋯	⋯	⋯	⋯	⋯	⋯	⋯
2MASS J16095361-1754474	Masking	0.00	2.73	4.00	3.68	3.11	1.78	⋯	⋯	⋯
2MASS J16095441-1906551	Imaging	⋯	⋯	⋯	⋯	⋯	⋯	4.00	5.00	7.00
2MASS J16095441-1906551	Coronagraph	⋯	⋯	⋯	⋯	⋯	⋯	⋯	⋯	⋯
2MASS J16095441-1906551	Masking	3.59	5.42	6.26	6.09	5.68	4.96	⋯	⋯	⋯
2MASS J16095933-1800090	Imaging	⋯	⋯	1.17	2.59	3.75	5.76	6.26	7.34	7.67
2MASS J16095933-1800090	Coronagraph	⋯	⋯	⋯	⋯	⋯	⋯	6.86	8.00	9.91
2MASS J16095933-1800090	Masking	0.24	3.24	4.27	3.96	3.38	2.23	⋯	⋯	⋯
2MASS J16101473-1919095	Imaging	⋯	⋯	0.14	1.59	3.16	1.93	5.98	7.58	8.39
2MASS J16101473-1919095	Coronagraph	⋯	⋯	⋯	⋯	⋯	⋯	⋯	⋯	⋯
2MASS J16101473-1919095	Masking	1.10	4.00	5.02	4.85	4.74	4.59	⋯	⋯	⋯
2MASS J16101888-2502325	Imaging	⋯	⋯	⋯	0.55	2.16	3.38	4.20	6.51	7.55
2MASS J16101888-2502325	Coronagraph	⋯	⋯	⋯	⋯	⋯	⋯	⋯	⋯	⋯
2MASS J16101888-2502325	Masking	⋯	⋯	⋯	⋯	⋯	⋯	⋯	⋯	⋯
2MASS J16102174-1904067	Imaging	⋯	⋯	⋯	⋯	⋯	⋯	4.00	5.00	7.00
2MASS J16102174-1904067	Coronagraph	⋯	⋯	⋯	⋯	⋯	⋯	⋯	⋯	⋯
2MASS J16102174-1904067	Masking	3.22	5.07	5.85	5.72	5.48	4.99	⋯	⋯	⋯
2MASS J16103956-1916524	Imaging	⋯	⋯	⋯	⋯	⋯	0.00	0.90	2.91	6.06
2MASS J16103956-1916524	Coronagraph	⋯	⋯	⋯	⋯	⋯	⋯	2.77	4.78	7.06
2MASS J16103956-1916524	Masking	0.00	0.00	0.78	0.58	0.00	0.00	⋯	⋯	⋯
2MASS J16104202-2101319	Imaging	⋯	⋯	⋯	⋯	⋯	⋯	4.00	5.00	8.00
2MASS J16104202-2101319	Coronagraph	⋯	⋯	⋯	⋯	⋯	⋯	⋯	⋯	⋯
2MASS J16104202-2101319	Masking	3.23	5.06	5.89	5.80	5.54	5.20	⋯	⋯	⋯
2MASS J16104636-1840598	Imaging	⋯	⋯	⋯	0.02	0.84	2.32	4.00	5.42	6.06
2MASS J16104636-1840598	Coronagraph	⋯	⋯	⋯	⋯	⋯	⋯	⋯	⋯	⋯
2MASS J16104636-1840598	Masking	0.00	1.06	2.62	2.24	1.41	0.13	⋯	⋯	⋯
2MASS J16111330-2019029	Imaging	⋯	⋯	2.38	5.01	5.75	7.02	7.57	7.89	8.06
2MASS J16111330-2019029	Coronagraph	⋯	⋯	⋯	⋯	⋯	⋯	7.53	8.78	10.95
2MASS J16111330-2019029	Masking	1.91	4.48	5.37	5.15	4.55	3.51	⋯	⋯	⋯
2MASS J16111534-1757214	Imaging	⋯	⋯	⋯	⋯	⋯	⋯	4.00	5.00	8.00
2MASS J16111534-1757214	Coronagraph	⋯	⋯	⋯	⋯	⋯	⋯	⋯	⋯	⋯
2MASS J16111534-1757214	Masking	3.80	5.63	6.45	6.31	6.15	5.72	⋯	⋯	⋯

Table 4
(Continued)

Primary	Technique	ΔK[a]								
		10–20	20–40	40–80	80–160	160–240	240–320	320–500	500–1000	>1000
2MASS J16111705-2213085	Imaging	⋯	⋯	2.26	3.89	4.94	7.03	7.57	8.65	8.98
2MASS J16111705-2213085	Coronagraph	⋯	⋯	⋯	⋯	⋯	⋯	⋯	⋯	⋯
2MASS J16111705-2213085	Masking	0.01	2.94	3.93	3.72	3.04	1.73	⋯	⋯	⋯
2MASS J16112057-1820549	Imaging	⋯	⋯	⋯	⋯	⋯	⋯	4.00	5.00	8.00
2MASS J16112057-1820549	Coronagraph	⋯	⋯	⋯	⋯	⋯	⋯	⋯	⋯	⋯
2MASS J16112057-1820549	Masking	⋯	3.28	4.86	5.28	5.23	⋯	⋯	⋯	⋯
2MASS J16115091-2012098	Imaging	⋯	⋯	2.21	3.94	5.14	6.72	7.95	7.94	8.00
2MASS J16115091-2012098	Coronagraph	⋯	⋯	⋯	⋯	⋯	⋯	8.08	8.54	10.17
2MASS J16115091-2012098	Masking	0.43	3.43	4.34	4.15	3.50	2.31	⋯	⋯	⋯
2MASS J16122737-2009596	Imaging	⋯	⋯	⋯	0.33	1.76	3.68	4.33	6.00	6.32
2MASS J16122737-2009596	Coronagraph	⋯	⋯	⋯	⋯	⋯	⋯	⋯	⋯	⋯
2MASS J16122737-2009596	Masking	0.00	1.12	2.66	2.32	1.55	0.13	⋯	⋯	⋯
2MASS J16123916-1859284	Imaging	⋯	⋯	1.58	3.21	5.10	3.57	7.67	7.87	8.25
2MASS J16123916-1859284	Coronagraph	⋯	⋯	⋯	⋯	⋯	⋯	7.55	8.72	11.65
2MASS J16123916-1859284	Masking	2.38	4.83	5.66	5.46	4.86	3.83	⋯	⋯	⋯
2MASS J16124893-1800525	Imaging	⋯	⋯	⋯	⋯	⋯	0.00	0.88	2.81	5.42
2MASS J16124893-1800525	Coronagraph	⋯	⋯	⋯	⋯	⋯	⋯	⋯	⋯	⋯
2MASS J16124893-1800525	Masking	⋯	⋯	⋯	⋯	⋯	⋯	⋯	⋯	⋯
2MASS J16125533-2319456	Imaging	⋯	⋯	⋯	0.26	1.47	3.16	3.97	4.99	6.08
2MASS J16125533-2319456	Coronagraph	⋯	⋯	⋯	⋯	⋯	⋯	1.66	2.53	6.97
2MASS J16125533-2319456	Masking	0.00	0.00	0.35	0.13	0.00	0.00	⋯	⋯	⋯
2MASS J16130996-1904269	Imaging	⋯	⋯	⋯	0.00	0.23	1.29	3.57	5.88	7.45
2MASS J16130996-1904269	Coronagraph	⋯	⋯	⋯	⋯	⋯	⋯	⋯	⋯	⋯
2MASS J16130996-1904269	Masking	0.00	2.24	3.65	3.37	2.67	1.26	⋯	⋯	⋯
2MASS J16142029-1906481	Imaging	⋯	⋯	⋯	3.09	4.00	4.60	5.80	7.20	10.20
2MASS J16142029-1906481	Coronagraph	⋯	⋯	⋯	⋯	⋯	⋯	⋯	⋯	⋯
2MASS J16142029-1906481	Masking	⋯	⋯	⋯	⋯	⋯	⋯	⋯	⋯	⋯
2MASS J16143367-1900133	Imaging	⋯	⋯	2.04	3.76	5.08	4.57	8.31	8.19	8.51
2MASS J16143367-1900133	Coronagraph	⋯	⋯	⋯	⋯	⋯	⋯	8.39	8.71	11.83
2MASS J16143367-1900133	Masking	2.69	5.09	5.95	5.75	5.15	4.16	⋯	⋯	⋯
2MASS J16145918-2750230	Imaging	⋯	⋯	2.74	4.34	5.14	5.84	6.24	7.90	8.49
2MASS J16145918-2750230	Coronagraph	⋯	⋯	⋯	⋯	⋯	⋯	8.04	9.26	11.80
2MASS J16145918-2750230	Masking	0.74	3.82	4.83	4.59	4.11	2.97	⋯	⋯	⋯
2MASS J16145928-2459308	Imaging	⋯	⋯	1.83	3.39	4.60	3.89	6.27	8.44	8.60
2MASS J16145928-2459308	Coronagraph	⋯	⋯	⋯	⋯	⋯	⋯	⋯	⋯	⋯
2MASS J16145928-2459308	Masking	0.56	3.60	4.60	4.35	3.88	2.90	⋯	⋯	⋯
2MASS J16151239-2420091	Imaging	⋯	⋯	0.34	1.76	3.05	4.05	6.39	7.21	7.68
2MASS J16151239-2420091	Coronagraph	⋯	⋯	⋯	⋯	⋯	⋯	⋯	⋯	⋯
2MASS J16151239-2420091	Masking	0.00	2.71	3.92	3.60	2.96	1.66	⋯	⋯	⋯
2MASS J16154416-1921171	Imaging	⋯	⋯	1.00	2.91	4.12	5.91	6.72	8.28	8.73
2MASS J16154416-1921171	Coronagraph	⋯	⋯	⋯	⋯	⋯	⋯	6.75	8.37	11.42
2MASS J16154416-1921171	Masking	2.39	4.83	5.78	5.58	4.92	3.89	⋯	⋯	⋯
2MASS J16163345-2521505	Imaging	⋯	⋯	2.23	3.99	5.20	7.47	8.18	8.33	8.45
2MASS J16163345-2521505	Coronagraph	⋯	⋯	⋯	⋯	⋯	⋯	8.20	8.74	10.63
2MASS J16163345-2521505	Masking	1.79	4.39	5.27	5.06	4.41	3.43	⋯	⋯	⋯
2MASS J16181904-2028479	Imaging	⋯	⋯	1.61	3.14	4.37	6.79	7.16	8.01	8.30
2MASS J16181904-2028479	Coronagraph	⋯	⋯	⋯	⋯	⋯	⋯	⋯	⋯	⋯
2MASS J16181904-2028479	Masking	0.16	3.14	4.25	3.90	3.35	2.22	⋯	⋯	⋯
2MASS J16215466-2043091	Imaging	⋯	⋯	⋯	⋯	⋯	⋯	4.00	5.00	8.00
2MASS J16215466-2043091	Coronagraph	⋯	⋯	⋯	⋯	⋯	⋯	⋯	⋯	⋯
2MASS J16215466-2043091	Masking	⋯	1.90	3.52	3.98	3.91	⋯	⋯	⋯	⋯
2MASS J16230783-2300596	Imaging	⋯	⋯	⋯	⋯	⋯	⋯	4.00	5.00	9.00
2MASS J16230783-2300596	Coronagraph	⋯	⋯	⋯	⋯	⋯	⋯	⋯	⋯	⋯
2MASS J16230783-2300596	Masking	⋯	3.31	4.87	5.18	5.08	⋯	⋯	⋯	⋯
2MASS J16235385-2946401	Imaging	⋯	⋯	⋯	0.09	0.99	2.05	3.50	4.70	5.40
2MASS J16235385-2946401	Coronagraph	⋯	⋯	⋯	⋯	⋯	⋯	0.91	2.06	6.30
2MASS J16235385-2946401	Masking	0.00	0.00	0.45	0.23	0.00	0.00	⋯	⋯	⋯
2MASS J16270942-2148457	Imaging	⋯	⋯	0.11	1.53	3.01	3.01	5.41	7.02	7.51
2MASS J16270942-2148457	Coronagraph	⋯	⋯	⋯	⋯	⋯	⋯	⋯	⋯	⋯
2MASS J16270942-2148457	Masking	0.00	0.39	1.75	1.36	0.49	0.00	⋯	⋯	⋯
2MASS J16294879-2137086	Imaging	⋯	⋯	⋯	⋯	0.03	0.84	3.59	5.18	6.23
2MASS J16294879-2137086	Coronagraph	⋯	⋯	⋯	⋯	⋯	⋯	⋯	⋯	⋯

Table 4
(Continued)

Primary	Technique	ΔK^{a}								
		10–20	20–40	40–80	80–160	160–240	240–320	320–500	500–1000	>1000
2MASS J16294879-2137086	Masking	⋯	⋯	⋯	⋯	⋯	⋯	⋯	⋯	⋯
2MASS J16303390-2428062	Imaging	⋯	⋯	0.53	2.09	3.37	5.17	6.47	7.13	7.37
2MASS J16303390-2428062	Coronagraph	⋯	⋯	⋯	⋯	⋯	⋯	6.51	7.70	9.39
2MASS J16303390-2428062	Masking	0.00	2.92	3.98	3.66	3.11	1.88	⋯	⋯	⋯
2MASS J16310240-2408431	Imaging	⋯	⋯	2.37	3.87	4.74	6.41	7.30	8.24	8.51
2MASS J16310240-2408431	Coronagraph	⋯	⋯	⋯	⋯	⋯	⋯	⋯	⋯	⋯
2MASS J16310240-2408431	Masking	0.06	3.01	4.13	3.79	3.24	2.09	⋯	⋯	⋯

Note.
[a] Separation bins are reported in units of mas and ΔK in units of magnitude.
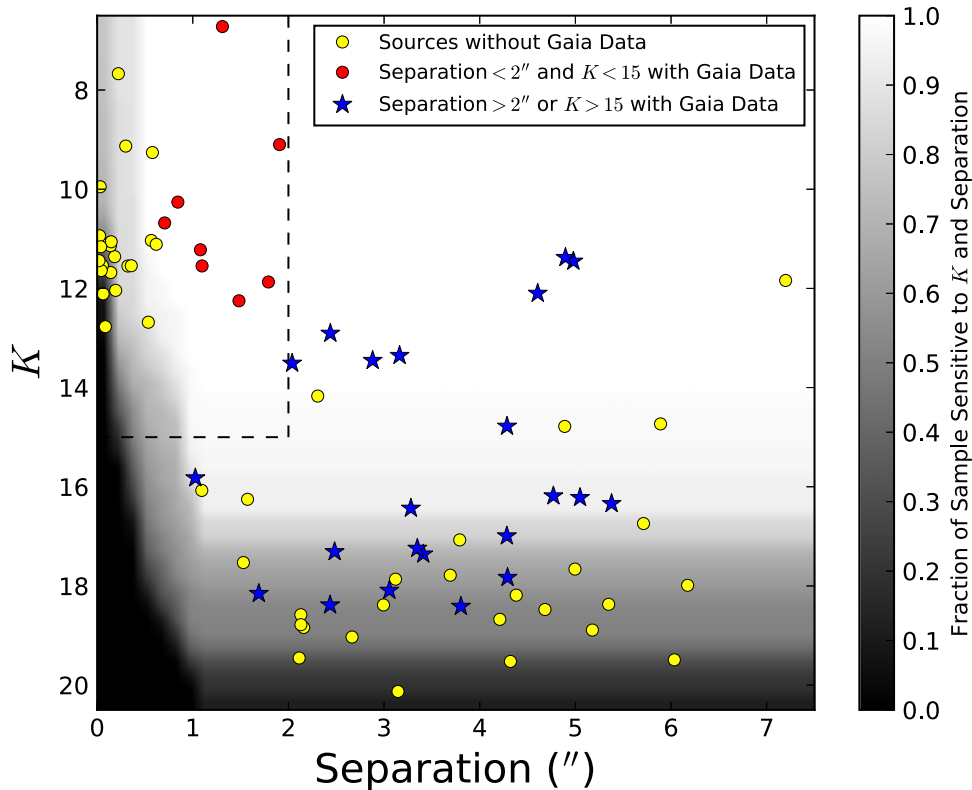
Figure 1. Projected separations and K magnitudes of the 79 detected sources around Upper Sco stars with disks. We consider sources within $2''$ and brighter than $K = 15$ to be candidate companions. This region is shown with dashed lines. A number of sources outside these limits may also be physically bound, but we expect significant background contamination among these sources. Red circles show sources that met our bound criteria and for which *Gaia* data were available, while blue stars show sources with *Gaia* data that did not meet our criteria. Sources with *Gaia* data are also shown in Figure 2. The yellow circles show sources for which no *Gaia* data were available. The grayscale background indicates the fraction of primary stars in the sample where the observations are sensitive to each K magnitude and separation.

3.4. Candidate Wide Companions with Gaia

To search for potential companions at wider projected separations, we used the *Gaia* DR2 Catalog to identify any sources within $1'$ of a target star of our Upper Sco disk sample. Figure 3 shows the *Gaia* parallaxes and proper motions of these sources. The majority of sources have parallaxes and proper motions concentrated close to zero, as expected for background objects. For each primary star in the sample, we searched for any additional sources with similar parallax and proper motions that stood out from the background sources. Figure 3 shows these candidate wide companions and primaries, which are clearly separated from the main cluster of background objects. These sources, listed in Table 5, have parallaxes within three milliarcseconds of their potential primaries and proper motions in R.A. and decl. within five milliarcseconds per year.

4. Disks and Multiplicity in Upper Sco

In this section, we describe the Upper Sco candidate companions discovered in our survey. We determine the locations of the millimeter disks in these systems relative to the primary and companion(s). We then compare the companion fractions of stars with and without disks in Upper Sco.
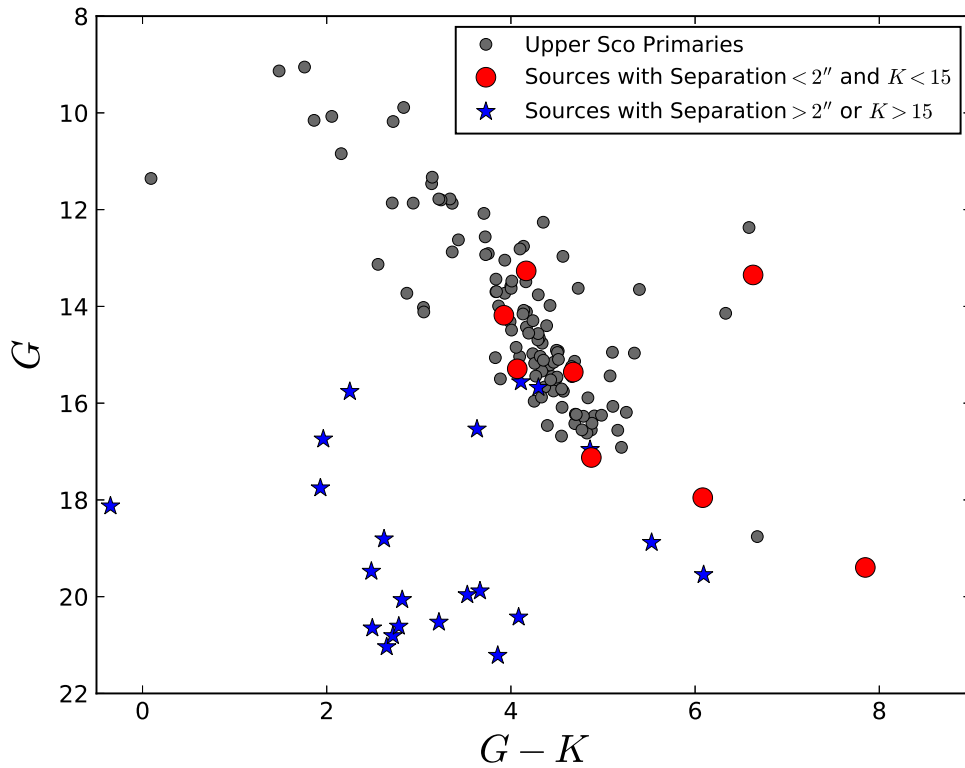
Figure 2. Color–magnitude diagram of Upper Sco primaries in our sample (gray points) and additional sources which meet (red circles) and fail to meet (blue stars) our criteria of separation $<2''$ and $K < 15$ to be considered candidate companions. Sources that meet our criteria lie along the same color–magnitude sequence as the Upper Sco primaries, as expected. Sources outside of these criteria are typically bluer and fainter than this sequence, consistent with background stars.
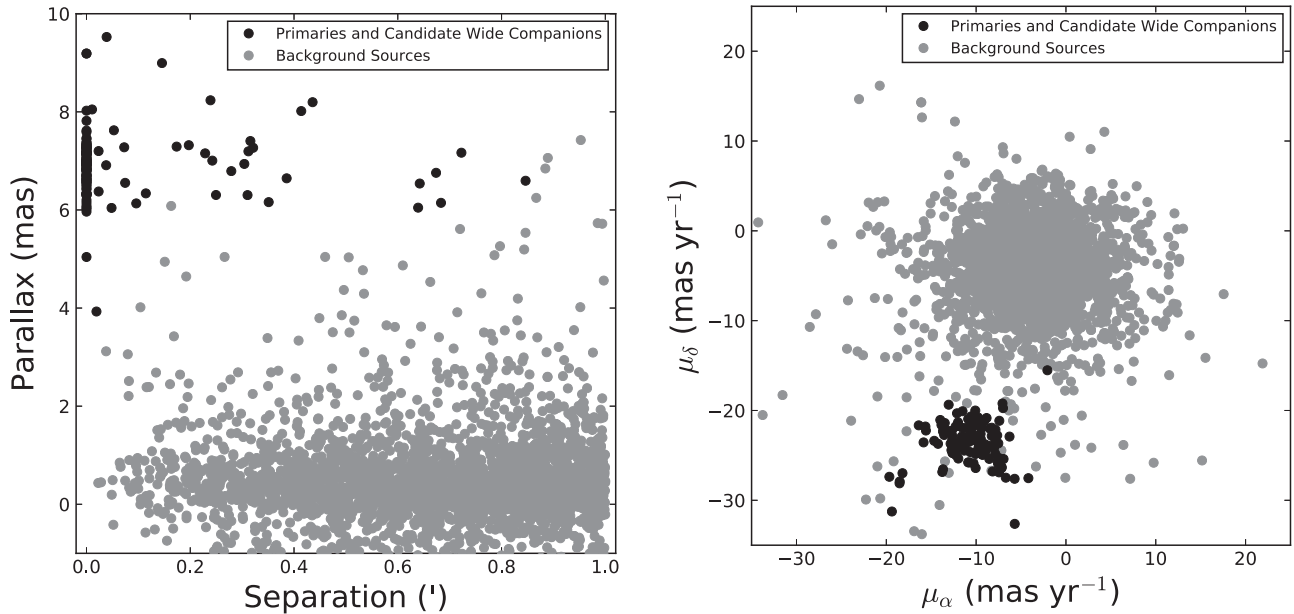
Figure 3. Parallaxes (left) and proper motions (right) of all sources in the *Gaia* DR2 Catalog within $1'$ of the targets in our Upper Sco disk sample. Most sources have parallaxes and proper motions close to zero, as expected for background objects. The black points show the primaries and candidate wide companions. The candidate wide companions have parallaxes and proper motions similar to their primaries and clearly distinct from the background sources.

4.1. Properties of Upper Sco Systems with Disks and Companions

We found 30 candidate companions in 27 systems brighter than $K = 15$ and with separations of less than $2''$. These include the previously known companions listed in Table 2 that meet these criteria. Newly discovered candidates are indicated

in Table 3 by the "Candidate Companion" column. Of the 81 primordial disk systems in the sample, 22 contain a candidate companion, along with five of the 31 debris/evolved transitional disks. The companions range in separation from $0''02$ to $1''91$, corresponding to projected separations of 2.8–265 au, assuming distances listed in Table 1. K-band magnitudes of

Table 5
Candidate Wide Companions from *Gaia*

System	Primary				Separation	Companion				
	G (mag)	μ_α (mas yr^{-1})	μ_δ (mas yr^{-1})	Parallax (mas)	(″)	Gaia Source Designation	G (mag)	μ_α (mas yr^{-1})	μ_δ (mas yr^{-1})	Parallax (mas)
2MASS J15551704-2322165	8.306 ± 0.001	−18.53 ± 0.12	−28.11 ± 0.07	8.24 ± 0.10	14.8989 ± 0.0807	6237252529183461248	13.491 ± 0.001	−19.66 ± 0.20	−27.38 ± 0.13	8.02 ± 0.11
2MASS J15551704-2322165	8.306 ± 0.001	−18.53 ± 0.12	−28.11 ± 0.07	8.24 ± 0.10	16.3749 ± 0.1173	6237252529183460992	14.150 ± 0.002	−18.20 ± 0.18	−26.98 ± 0.12	8.02 ± 0.09
2MASS J15551704-2322165	8.306 ± 0.001	−18.53 ± 0.12	−28.11 ± 0.07	8.24 ± 0.10	17.9029 ± 0.1522	6237252529178690432	15.393 ± 0.006	−18.51 ± 0.29	−27.91 ± 0.18	8.20 ± 0.14
2MASS J15554883-2512240	10.155 ± 0.002	−15.85 ± 0.10	−23.56 ± 0.06	6.95 ± 0.05	8.8551 ± 0.1552	6235742349962814592	13.918 ± 0.001	−15.59 ± 0.44	−22.23 ± 0.26	8.99 ± 0.22
2MASS J15554883-2512240	10.155 ± 0.002	−15.85 ± 0.10	−23.56 ± 0.06	6.95 ± 0.05	14.5251 ± 0.1366	6235742349962814848	16.898 ± 0.005	−15.64 ± 0.31	−21.79 ± 0.18	7.01 ± 0.16
2MASS J16014086-2258103	14.948 ± 0.019	−8.80 ± 0.26	−24.20 ± 0.12	8.05 ± 0.10	0.6950 ± 0.0936	6243135809748290688	15.357 ± 0.001	−13.77 ± 0.52	−26.85 ± 0.20	9.19 ± 0.43
2MASS J16025123-2401574	11.866 ± 0.003	−11.85 ± 0.12	−24.03 ± 0.05	6.95 ± 0.07	7.2151 ± 0.0837	6236273895118890112	16.364 ± 0.001	−12.70 ± 0.32	−23.87 ± 0.19	6.34 ± 0.20
2MASS J16035767-2031055	12.078 ± 0.003	−11.60 ± 0.08	−22.90 ± 0.04	7.01 ± 0.04	50.2880 ± 0.1497	6244083039015457152	12.298 ± 0.002	−10.51 ± 0.34	−21.64 ± 0.22	6.60 ± 0.22
2MASS J16041740-1942287	14.761 ± 0.002	−9.70 ± 0.19	−21.63 ± 0.09	6.20 ± 0.09	5.4847 ± 0.0888	6247221285718007680	15.561 ± 0.001	−9.13 ± 0.23	−21.16 ± 0.11	6.13 ± 0.11
2MASS J16041740-1942287	14.761 ± 0.002	−9.70 ± 0.19	−21.63 ± 0.09	6.20 ± 0.09	38.7849 ± 0.0886	6247227161233273088	17.272 ± 0.002	−8.26 ± 0.33	−22.83 ± 0.16	6.05 ± 0.17
2MASS J16042165-2130284	11.868 ± 0.016	−12.33 ± 0.10	−23.83 ± 0.05	6.66 ± 0.06	16.2112 ± 0.0666	6243393817024156288	13.607 ± 0.002	−12.64 ± 0.18	−24.73 ± 0.09	6.79 ± 0.10
2MASS J16061144-1935405	15.748 ± 0.001	−11.94 ± 0.33	−21.73 ± 0.19	7.29 ± 0.14	10.7768 ± 0.1387	6247238293789181440	16.552 ± 0.004	−11.52 ± 0.35	−21.94 ± 0.20	7.17 ± 0.14
2MASS J16070014-2033092	13.781 ± 0.001	−13.86 ± 0.18	−21.61 ± 0.13	7.32 ± 0.10	11.8052 ± 0.1059	6244106163113915904	14.082 ± 0.002	−13.28 ± 0.16	−22.22 ± 0.11	7.18 ± 0.09
2MASS J16070211-2019387	16.560 ± 0.003	−9.99 ± 0.36	−21.41 ± 0.24	6.70 ± 0.22	1.4975 ± 0.3257	6244125331552799488	17.123 ± 0.011	−9.96 ± 0.71	−20.95 ± 0.53	3.93 ± 0.42
2MASS J16070873-1927341	13.732 ± 0.001	−10.55 ± 0.27	−20.66 ± 0.19	6.64 ± 0.14	23.4170 ± 0.1070	6247244203663970944	15.442 ± 0.001	−9.92 ± 0.19	−21.43 ± 0.13	6.84 ± 0.09
	14.115 ± 0.048	−7.15 ± 0.26	−26.31 ± 0.18	5.04 ± 0.20	41.0394 ± 0.1838	6243914435774449280	15.974 ± 0.001	−9.50 ± 0.33	−22.61 ± 0.17	6.15 ± 0.20

Table 5
(Continued)

System	Primary				Separation (″)	Companion				
	G (mag)	μ_α (mas yr^{-1})	μ_δ (mas yr^{-1})	Parallax (mas)		Gaia Source Designation	G (mag)	μ_α (mas yr^{-1})	μ_δ (mas yr^{-1})	Parallax (mas)
2MASS J16075796-2040087										
2MASS J16075796-2040087	14.115 ± 0.048	−7.15 ± 0.26	−26.31 ± 0.18	5.04 ± 0.20	14.5344 ± 0.2013	6243914607573142784	16.440 ± 0.002	−10.29 ± 0.35	−25.90 ± 0.24	6.31 ± 0.25
2MASS J16075796-2040087	14.115 ± 0.048	−7.15 ± 0.26	−26.31 ± 0.18	5.04 ± 0.20	21.5220 ± 0.1492	6243914641932881664	17.557 ± 0.002	−9.68 ± 0.42	−22.91 ± 0.27	6.16 ± 0.28
2MASS J16082324-1930009	12.823 ± 0.002	−12.27 ± 0.11	−21.78 ± 0.08	7.15 ± 0.05	13.4420 ± 0.0659	6245739521996902272	13.131 ± 0.007	−12.70 ± 0.12	−22.26 ± 0.09	7.25 ± 0.06
2MASS J16090002-1908368[a]	12.908 ± 0.007	−9.29 ± 0.14	−24.92 ± 0.09	7.27 ± 0.08	18.9511 ± 0.0874	6245777283349431552	15.462 ± 0.001	−10.04 ± 0.23	−24.81 ± 0.16	7.19 ± 0.14
2MASS J16090075-1908526[a]	12.908 ± 0.007	−9.29 ± 0.14	−24.92 ± 0.09	7.27 ± 0.08	18.9511 ± 0.0874	6245777283349431552	15.462 ± 0.001	−10.04 ± 0.23	−24.81 ± 0.16	7.19 ± 0.14
2MASS J16101888-2502325	11.356 ± 0.002	−10.76 ± 0.16	−23.49 ± 0.11	6.55 ± 0.08	4.9015 ± 0.1327	6049748786908497408	15.677 ± 0.001	−10.06 ± 0.30	−24.64 ± 0.23	6.42 ± 0.16
2MASS J16102174-1904067	13.627 ± 0.002	−9.41 ± 0.14	−24.07 ± 0.10	7.46 ± 0.06	4.6059 ± 0.0780	6245781131640479360	16.959 ± 0.002	−9.25 ± 0.36	−24.76 ± 0.23	7.28 ± 0.15
2MASS J16104202-2101319	11.799 ± 0.004	−9.82 ± 0.11	−23.34 ± 0.07	7.14 ± 0.05	3.2033 ± 0.2418	6243833724749589760	15.517 ± 0.002	−10.89 ± 0.61	−25.78 ± 0.38	7.62 ± 0.27
2MASS J16111330-2019029	13.981 ± 0.016	−7.84 ± 0.10	−22.13 ± 0.07	6.44 ± 0.06	18.3302 ± 0.0765	6243940617895463296	14.818 ± 0.003	−7.65 ± 0.20	−22.77 ± 0.13	6.30 ± 0.13
2MASS J16111534-1757214	12.930 ± 0.002	−9.12 ± 0.12	−24.75 ± 0.09	7.33 ± 0.06	40.4631 ± 0.2150	6249001841715440512	13.692 ± 0.003	−7.53 ± 0.49	−23.66 ± 0.36	6.76 ± 0.27
2MASS J16113134-1838259	12.370 ± 0.042	−7.45 ± 0.20	−26.89 ± 0.14	7.82 ± 0.10	1.3123 ± 0.1477	6245891976152406016	13.350 ± 0.035	−9.48 ± 0.47	−23.17 ± 0.43	6.38 ± 0.19
2MASS J16123916-1859284	10.396 ± 0.002	−8.26 ± 0.11	−21.92 ± 0.08	7.40 ± 0.05	19.1170 ± 0.0838	6245821092014031616	13.045 ± 0.005	−8.54 ± 0.16	−25.39 ± 0.11	7.19 ± 0.08
2MASS J16124893-1800525	14.553 ± 0.001	−7.42 ± 0.16	−21.15 ± 0.11	6.32 ± 0.07	3.1844 ± 0.1887	6249313690697472512	18.881 ± 0.003	−7.00 ± 0.70	−19.74 ± 0.51	6.04 ± 0.32
2MASS J16125533-2319456	9.053 ± 0.001	−9.56 ± 0.11	−23.63 ± 0.07	6.57 ± 0.04	38.3021 ± 0.0526	6242176829446854656	11.763 ± 0.002	−8.32 ± 0.10	−23.92 ± 0.07	6.54 ± 0.04
	13.235 ± 0.011	−8.17 ± 0.13	−26.79 ± 0.09	7.17 ± 0.07	43.7319 ± 0.0681	6245801816200921088	14.143 ± 0.034	−7.16 ± 0.22	−26.40 ± 0.16	6.99 ± 0.12

Table 5
(Continued)

System	Primary				Separation ('')	Companion				
	G (mag)	μ_α (mas yr^{-1})	μ_δ (mas yr^{-1})	Parallax (mas)		Gaia Source Designation	G (mag)	μ_α (mas yr^{-1})	μ_δ (mas yr^{-1})	Parallax (mas)
2MASS J16142029-1906481										
2MASS J16151239-2420091	16.680 ± 0.001	-12.13 ± 0.24	-20.31 ± 0.16	6.51 ± 0.13	17.8773 ± 0.1938	6049726040762143488	18.124 ± 0.002	-11.51 ± 0.45	-20.08 ± 0.31	6.94 ± 0.22
2MASS J16153456-2242421	12.260 ± 0.004	-7.55 ± 0.11	-25.94 ± 0.07	7.16 ± 0.04	1.9157 ± 0.0375	6242598526515738112	13.266 ± 0.001	-10.05 ± 0.16	-26.41 ± 0.07	7.20 ± 0.05
2MASS J16220961-1953005	13.626 ± 0.001	-5.72 ± 0.21	-27.61 ± 0.13	7.22 ± 0.10	1.7979 ± 0.4106	6245095242538868992	17.954 ± 0.005	-7.52 ± 1.02	-25.38 ± 0.70	9.53 ± 0.56
2MASS J16220961-1953005	13.626 ± 0.001	-5.72 ± 0.21	-27.61 ± 0.13	7.22 ± 0.10	2.8881 ± 0.2891	6245095345618083968	19.546 ± 0.007	-4.18 ± 1.81	-27.54 ± 1.03	6.91 ± 0.71

Note.

[a] 2MASS J16090002-1908368 and 2MASS J16090075-1908526 are a 18''9511 pair with matching parallaxes and proper motions.
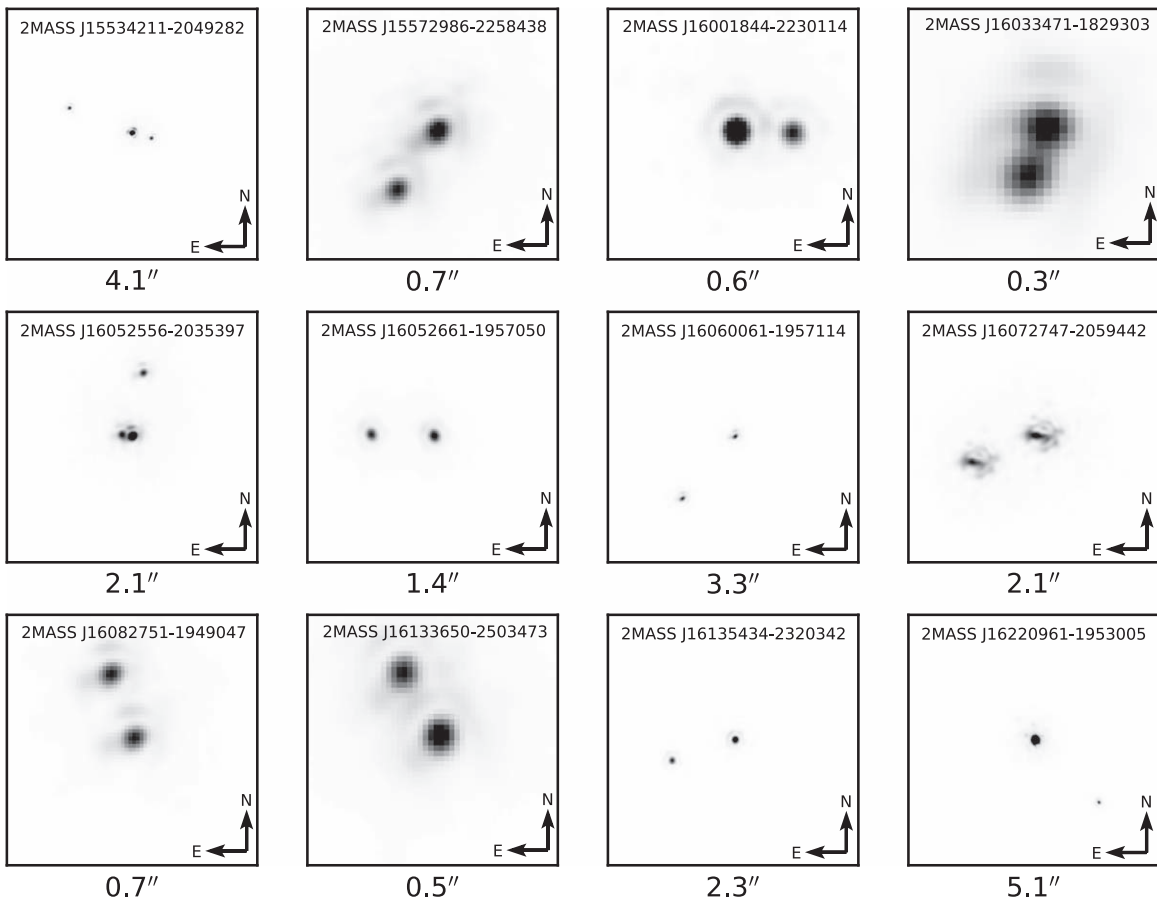
Figure 4. NIRC2 K' images of the Upper Sco disk systems with new companions discovered by imaging in this survey. The angular extent of each image is indicated for each panel.

these objects range from 6.72 to 12.77. NIRC2 K' images of the 12 systems with new companions discovered by imaging are shown in Figure 4. Ten of these systems include a single candidate companion, while two targets, 2MASS J15534211-2049282 and 2MASS J16052556-2035397, appear to be triple systems.

Figure 5 shows ALMA 880 μm continuum images of the 26 systems with companions for which we have ALMA data (Barenfeld et al. 2016). These exclude 2MASS J16033471-1829303, an M5 star with a disk identified by infrared excess (Luhman & Mamajek 2012) that was not observed with ALMA. The relative positions of the primary and companion(s) are overlaid in each image. The locations of the primary stars at the time of the ALMA observations were calculated using positions and proper motions from the *Gaia* DR2 Catalog. When *Gaia* proper motions or positions were unavailable, we used data from the PPMXL catalog (Roeser et al. 2010). For 16 systems, the millimeter emission is only at the location of the primary star or is not detected toward either component. Individual disks are detected around each component of 2MASS J16113134-1838259 and 2MASS J16135434-2320342. The disk in 2MASS J16052556-2035397 appears to be located around the wider companion of this triple system. This may also be the case for 2MASS J16082751-1949047. However, the uncertainties of the R.A. and decl. of the primary star are 0″11 due to only data from PPMXL being available for this system. We therefore cannot definitively determine the

relative positions of the disk and stars. Six other systems, 2MASS J15534211-2049282, 2MASS J16001844-2230114, 2MASS J16043916-1942459, 2MASS J16075796-2040087, 2MASS J16133650-2503473, and 2MASS J16141107-2305362, show disk millimeter emission that encompasses both stellar components at the resolution of the ALMA observations. The disks in 2MASS J16082751-1949047 and these six other systems may exist around one or both stars individually or may be circumbinary.

Figure 6 shows the infrared spectral energy distributions (SEDs) of the seven systems where the millimeter-wavelength emission cannot be conclusively assigned to the primary or secondary given the angular resolution of the ALMA observations. Infrared photometry is from 2MASS (Cutri et al. 2003), *Spitzer*, and *WISE* (Luhman & Mamajek 2012). Stellar photospheres were estimated assuming blackbody emission with the same stellar parameters as in Barenfeld et al. (2016). Six systems show infrared excess at wavelengths shorter than 10 μm, indicating the presence of warm dust. This does not necessarily rule out circumbinary disks, but we can say that there must be dust around one or both individual stars. Since 2MASS J16043916-1942459 exhibits an infrared excess only at 24 μm and has a companion with a projected separation of only 3.8 au, this system is likely to be a circumbinary disk. However, given the weakness of the 24 μm excess and low S/N of the ALMA image, its nature is difficult to determine with certainty.
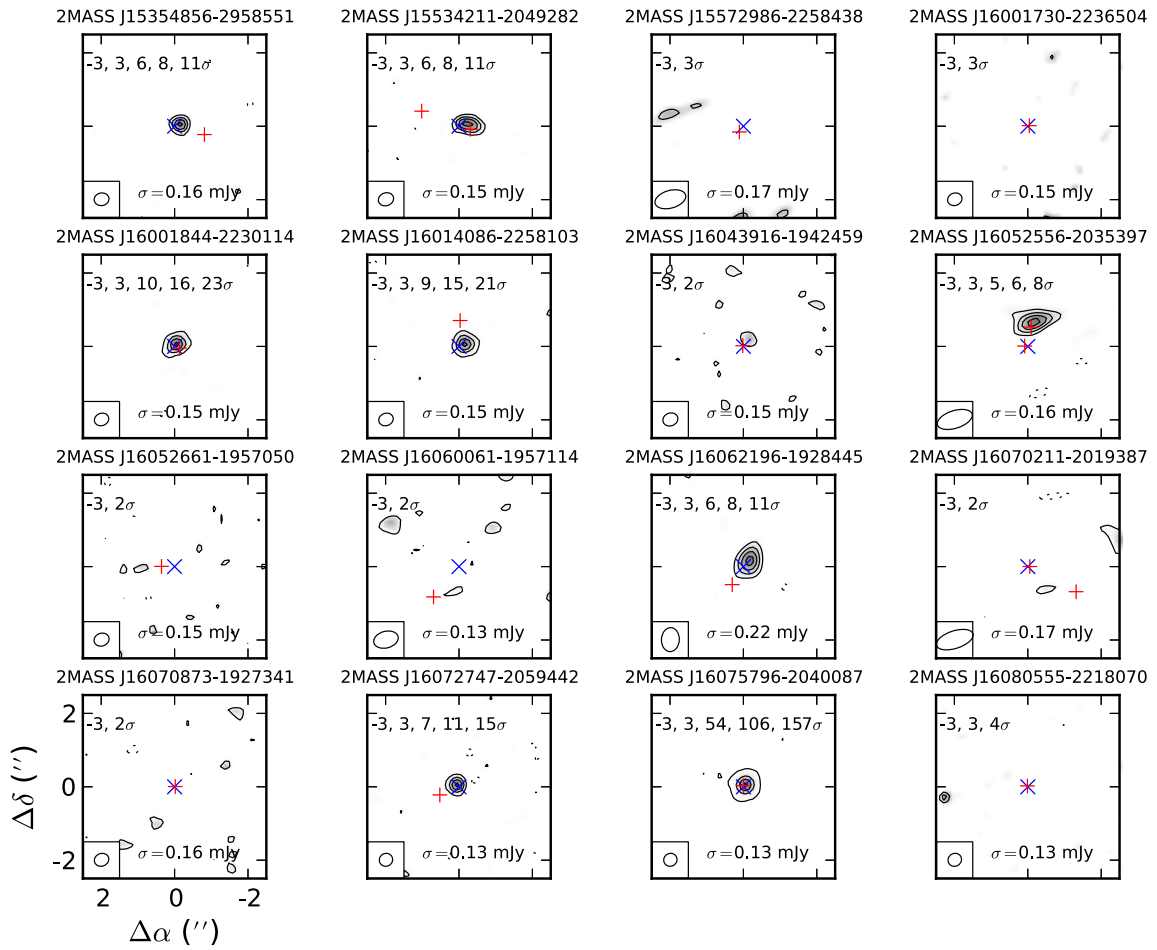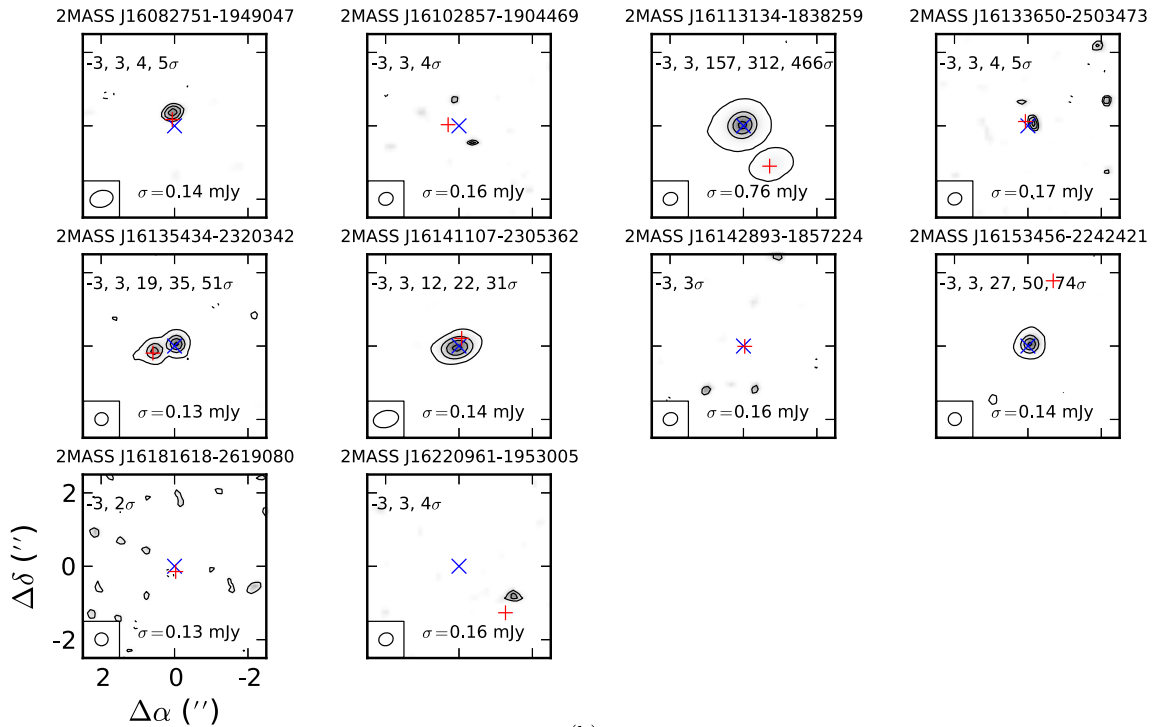
Figure 5. ALMA 880 μm continuum images of the Upper Sco systems with disks and companions in this sample. These exclude 2MASS J16033471-1829303, which was not observed with ALMA. The relative positions of the primary (blue "X") and companion(s) (red "+") are overlaid. Spectral energy distributions of the seven sources where the millimeter-wavelength emission cannot be conclusively assigned to the primary or secondary are shown in Figure 6.
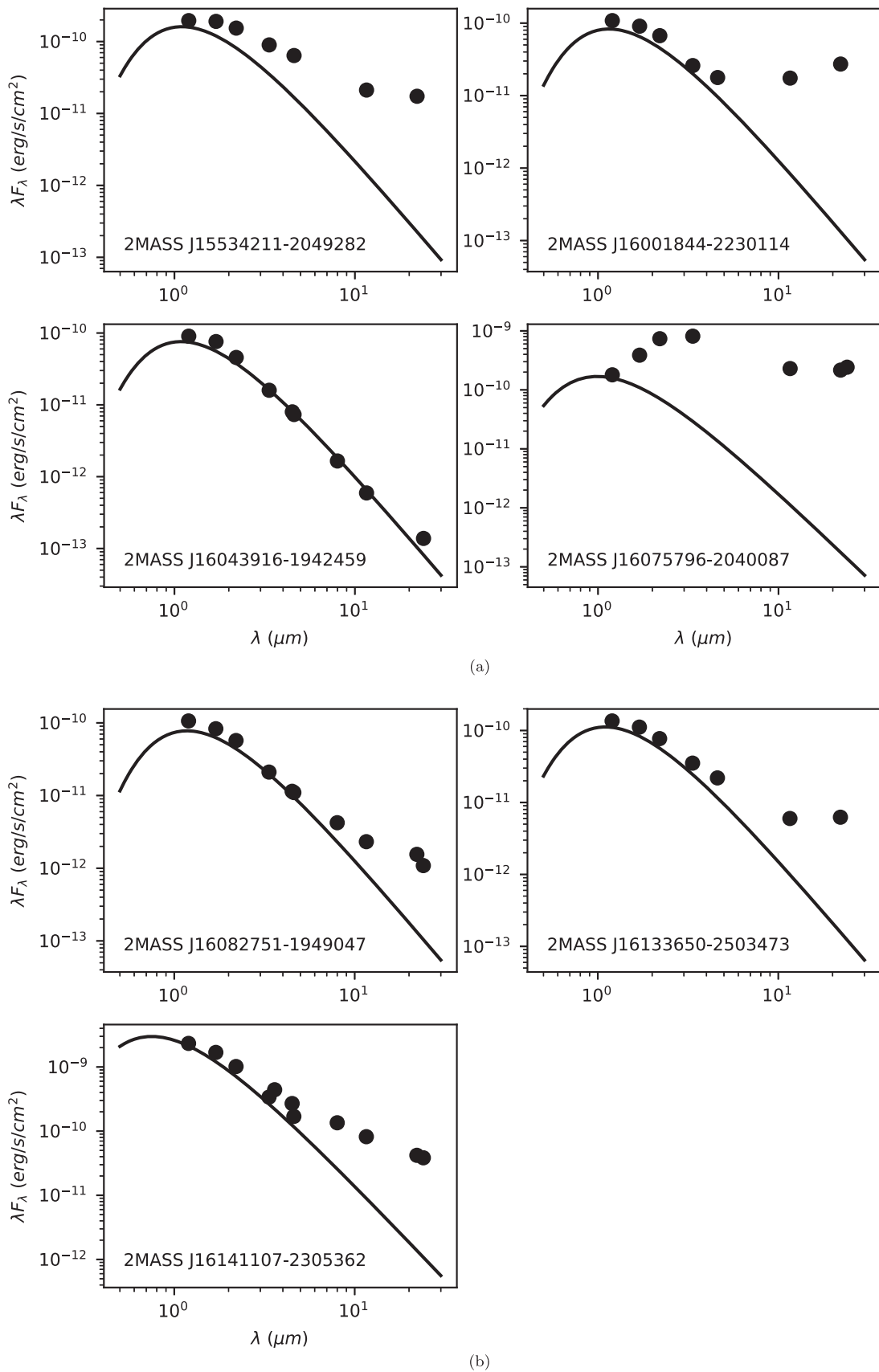
Figure 6. Infrared spectral energy distributions of the systems in Figure 5 for which the millimeter-wavelength emission cannot be conclusively assigned to the primary or secondary. Stellar photospheric emission is estimated assuming blackbody emission with the stellar parameters calculated in Barenfeld et al. (2016). With the exception of 2MASS J16043916-1942459, all systems show excess at wavelengths ⩽8 μm, indicating that warm dust is present around the primary and/or companion(s) in these systems.

Table 6
Upper Sco Systems without Disks

Primary	Spectral Type	K_{prim}[a] (mag)	Separation[b] (mas)	ΔK[c] (mag)	K_{comp}[c] (mag)	Position Angle[c] (deg)
2MASS J15355780-2324046	K3	9.43 ± 0.02	54.68 ± 0.16	2.97 ± 0.01	12.40 ± 0.05	173.76 ± 0.19
2MASS J15500499-2311537	M2	8.93 ± 0.02	26.93 ± 0.04	0.76 ± 0.04	9.69 ± 0.07	222.07 ± 0.11
2MASS J15505641–2534189	G0	7.91 ± 0.02	128 ± 1	0.03 ± 0.01	7.94 ± 0.05	72.70 ± 0.06
2MASS J15510660-2402190	M2	9.73 ± 0.02	⋯	⋯	⋯	⋯
2MASS J15545986-2347181	G3	7.03 ± 0.02	766 ± 3	1.99 ± 0.01	9.02 ± 0.05	232.0 ± 0.1
2MASS J15562941–2348197	M1.5	8.75 ± 0.02	92 ± 6	0.62 ± 0.05	9.37 ± 0.07	169.8 ± 5.0
2MASS J15565545-2258403	M0	9.43 ± 0.02	⋯	⋯	⋯	⋯
2MASS J15570234-1950419	K7	8.37 ± 0.02	558 ± 1	0.54 ± 0.01	8.91 ± 0.05	292.1 ± 0.3
2MASS J15571998-2338499	M0	8.88 ± 0.02	124 ± 1	0.58 ± 0.02	9.46 ± 0.06	166.5 ± 0.4
2MASS J15572575-2354220	M0.5	9.09 ± 0.03	1324 ± 3	0.63 ± 0.12	9.72 ± 0.13	226.0 ± 0.4
2MASS J15573430-2321123	M1	8.99 ± 0.02	53.86 ± 0.19	0.78 ± 0.01	9.77 ± 0.05	68.93 ± 0.20
2MASS J15575002-2305094	M0	9.27 ± 0.02	⋯	⋯	⋯	⋯
2MASS J15590208-1844142	K6.5	8.11 ± 0.02	846 ± 1	0.85 ± 0.01	8.96 ± 0.05	58.0 ± 0.1
2MASS J15595995-2220367	M1	8.63 ± 0.02	25.40 ± 0.12	0.03 ± 0.01	8.66 ± 0.05	113.55 ± 0.62
2MASS J16003134-2027050	M1	8.83 ± 0.02	189 ± 4	0.43 ± 0.04	9.26 ± 0.07	171.7 ± 0.5
2MASS J16004056-2200322	G9	8.44 ± 0.02	⋯	⋯	⋯	⋯
2MASS J16004277-2127380	K8	8.92 ± 0.02	⋯	⋯	⋯	⋯
2MASS J16010519-2227311	M3	8.75 ± 0.02	193 ± 5	0.60 ± 0.11	9.35 ± 0.12	313.7 ± 1.2
2MASS J16010801–2113184	K8	8.80 ± 0.02	⋯	⋯	⋯	⋯
2MASS J16012563-2240403	K3	8.52 ± 0.02	⋯	⋯	⋯	⋯
2MASS J16014743-2049457	M0	8.61 ± 0.02	205 ± 3	0.58 ± 0.03	9.19 ± 0.06	324.7 ± 0.9
2MASS J16015149-2445249	K7	8.49 ± 0.03	76 ± 5	1.00 ± 0.07	9.49 ± 0.09	289.6 ± 10.0
2MASS J16015822-2008121	G7	7.67 ± 0.02	39.31 ± 1.57	2.14 ± 0.13	9.81 ± 0.14	217.67 ± 0.59
2MASS J16020845-2254588	M1	9.55 ± 0.02	⋯	⋯	⋯	⋯
2MASS J16021045-2241280	K6	8.06 ± 0.03	300 ± 3	0.65 ± 0.02	8.71 ± 0.06	346.0 ± 0.3
2MASS J16025243-2402226	K0	7.65 ± 0.02	⋯	⋯	⋯	⋯
2MASS J16025396-2022480	K6	8.19 ± 0.03	310 ± 8	0.18 ± 0.07	8.37 ± 0.09	5.3 ± 0.3
2MASS J16030269-1806050	K6	8.73 ± 0.02	⋯	⋯	⋯	⋯
2MASS J16032367-1751422	M2	8.61 ± 0.03	⋯	⋯	⋯	⋯
2MASS J16033550-2245560	K0	8.36 ± 0.02	⋯	⋯	⋯	⋯
2MASS J16034187-2005577	M2	9.49 ± 0.02	⋯	⋯	⋯	⋯
2MASS J16034334-2015314	M2	9.72 ± 0.02	⋯	⋯	⋯	⋯
2MASS J16035496-2031383	M0	8.62 ± 0.02	121 ± 3	0.53 ± 0.04	9.15 ± 0.07	140.9 ± 0.6
2MASS J16042839-1904413	M3	9.28 ± 0.02	881 ± 1	0.04 ± 0.01	9.32 ± 0.05	128.13 ± 0.10
2MASS J16044776-1930230	K2.5	8.04 ± 0.02	43.18 ± 0.12	0.70 ± 0.03	8.74 ± 0.06	68.63 ± 0.29
2MASS J16051791-2024195	M3	9.14 ± 0.02	16.15 ± 0.59	0.40 ± 0.07	9.54 ± 0.09	251.12 ± 1.11
2MASS J16052726-1938466	M1	9.55 ± 0.02	⋯	⋯	⋯	⋯
2MASS J16053936-2152338	M3.5	9.47 ± 0.02	⋯	⋯	⋯	⋯
2MASS J16054266-2004150	M2	9.16 ± 0.03	643 ± 3	0.56 ± 0.03	9.72 ± 0.07	352.6 ± 0.4
2MASS J16061254-2036472	K5	8.90 ± 0.02	⋯	⋯	⋯	⋯
2MASS J16063169-2036232	K6	8.73 ± 0.02	⋯	⋯	⋯	⋯
2MASS J16063741–2108404	M1	9.11 ± 0.03	1279 ± 3	0.09 ± 0.01	9.20 ± 0.06	33.9 ± 0.3
2MASS J16065436-2416107	M3	8.86 ± 0.03	1500 ± 500	1.3 ± 0.5	10.2 ± 0.5	270 ± 9
2MASS J16070356-2036264	M0	8.10 ± 0.02	184 ± 1	0.15 ± 0.03	8.25 ± 0.06	344.2 ± 0.3
2MASS J16070373-2043074	M2	9.53 ± 0.02	⋯	⋯	⋯	⋯
2MASS J16070393-1911338	M1	9.22 ± 0.03	599 ± 3	1.47 ± 0.01	10.69 ± 0.06	87.6 ± 0.3
2MASS J16070767-1927161	M2	9.80 ± 0.02	105.25 ± 0.21	2.33 ± 0.01	12.13 ± 0.05	0.90 ± 0.09
2MASS J16080141-2027416	K8	9.29 ± 0.02	⋯	⋯	⋯	⋯
2MASS J16081474-1908327	K2	8.43 ± 0.02	24.6 ± 5.2	2.44 ± 1.16	10.87 ± 1.16	42.5 ± 3.6
2MASS J16082234-1930052	M1	9.06 ± 0.02	⋯	⋯	⋯	⋯
2MASS J16082387-1935518	M1	9.25 ± 0.02	652 ± 1	0.98 ± 0.01	10.23 ± 0.05	65.61 ± 0.11
2MASS J16082511-2012245	M1	9.87 ± 0.02	⋯	⋯	⋯	⋯
2MASS J16083138-1802414	M0	8.91 ± 0.02	⋯	⋯	⋯	⋯
2MASS J16085673-2033460	K5	8.62 ± 0.02	⋯	⋯	⋯	⋯
2MASS J16090844-2009277	M4	9.52 ± 0.03	⋯	⋯	⋯	⋯
2MASS J16091684-1835226	M2	9.67 ± 0.02	⋯	⋯	⋯	⋯
2MASS J16093030-2104589	M0	8.92 ± 0.02	⋯	⋯	⋯	⋯
2MASS J16094644-1937361	M1	9.63 ± 0.02	⋯	⋯	⋯	⋯
2MASS J16103196-1913062	K7	8.99 ± 0.02	145.55 ± 0.43	2.96 ± 0.02	11.95 ± 0.06	81.63 ± 0.14
2MASS J16110890-1904468	K2	7.69 ± 0.02	⋯	⋯	⋯	⋯
2MASS J16115633-2304051	M1	8.82 ± 0.03	1981 ± 4	0.37 ± 0.01	9.19 ± 0.06	155.29 ± 0.06
2MASS J16115927-1906532	K0	8.09 ± 0.03	⋯	⋯	⋯	⋯
2MASS J16124051-1859282	K6	7.49 ± 0.02	144 ± 5	1.10 ± 0.10	8.59 ± 0.11	162.15 ± 1.76

Table 6
(Continued)

Primary	Spectral Type	K_{prim}[a] (mag)	Separation[b] (mas)	ΔK[c] (mag)	K_{comp}[c] (mag)	Position Angle[c] (deg)
2MASS J16130271–2257446	K4.5	8.46 ± 0.03	…	…	…	…
2MASS J16131858-2212489	K0	7.43 ± 0.02	…	…	…	…
2MASS J16132929-2311075	K1	8.49 ± 0.02	1430 ± 2	2.70 ± 0.05	11.19 ± 0.07	91.41 ± 0.05
2MASS J16134750-1835004	M2	9.91 ± 0.02	…	…	…	…
2MASS J16135815-1848290	M2	9.88 ± 0.02	…	…	…	…
2MASS J16140211–2301021	G4	8.61 ± 0.02	…	…	…	…
2MASS J16161795-2339476	G8	8.10 ± 0.02	…	…	…	…
2MASS J16173138-2303360	G1	7.97 ± 0.03	…	…	…	…
2MASS J16193396-2228294	K0.5	8.51 ± 0.02	…	…	…	…
2MASS J16204596-2348208	K3	8.93 ± 0.02	…	…	…	…
2MASS J16245136-2239325	G7	7.08 ± 0.02	44.30 ± 0.07	0.45 ± 0.01	7.53 ± 0.05	230.74 ± 0.08
2MASS J16273956-2245230	K2	8.08 ± 0.03	…	…	…	…
2MASS J16294869-2152118	K2	7.76 ± 0.02	…	…	…	…
2MASS J16354836-2148396	M0	8.48 ± 0.02	…	…	…	…

Notes.
[a] Primary K magnitude.
[b] Ellipses indicate single stars.
[c] ΔK, K_{comp}, and position angle are defined as in Table 2.
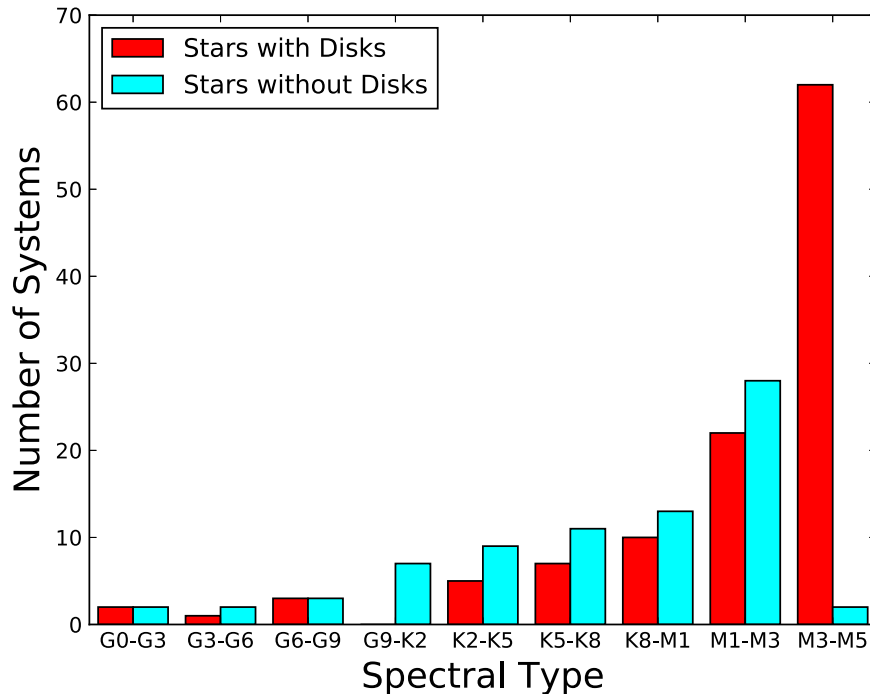
Figure 7. Spectral-type distributions of Upper Sco primary stars with (red) and without (cyan) disks. This disk sample includes 62 systems with spectral types later than M3, compared to only two such systems without disks. Restricting to spectral types M3 and earlier, the samples are consistent with being drawn from the same parent distribution.

4.2. A Comparison of Upper Sco Systems with and without Disks

We now compare the stellar companion fraction for Upper Sco stars with and without circumstellar disks. As described in Section 3, we have detected 30 candidate companions brighter than $K = 15$ and with separations of less than 2″ in 27 of 112 systems with disks identified from infrared colors (see Section 2). Our comparison sample is composed of the 77 Upper Sco stars without those disks surveyed for stellar companions by Kraus et al. (2008) using similar observations to those presented here. This sample, listed in Table 6, ranges

in spectral type from G0 to M4 (inclusive) and is described in detail by Kraus et al. (2008). Companions identified in this sample meet the same brightness and separation criteria used in this work.

To ensure a meaningful comparison of systems with and without disks, we examined the spectral-type distributions of these samples. The distributions of primary star spectral types for the two samples are shown in Figure 7. Only two of the 77 systems without disks have spectral types later than M3, compared to 62 of the 112 systems in the disk sample. The latter sample was extended to later spectral types in order to
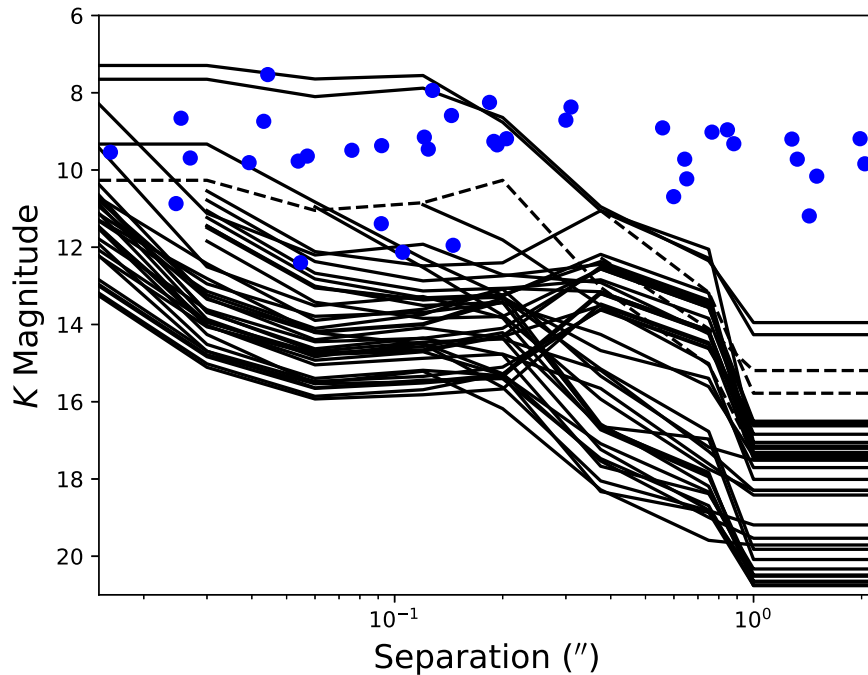
Figure 8. Apparent magnitude detection limits as a function of separation for Upper Sco disk-hosts with no candidate companions and spectral types of M3 or earlier. The dashed curves show the contrast limits for the three sources with poor tip-tilt in this spectral type range. The blue points show the companions found by Kraus et al. (2008) among a sample of Upper Sco stars without disks. The majority of observations in the current disk sample were sensitive enough to have detected all of these companions if they were present around the disk-hosting stars. Under the assumption that the stars with disks have the same population of companions as those without disks, we would have only expected to miss approximately two to three of these companions due to lower sensitivities.

include a larger number of Upper Sco systems with disks in the studies by Barenfeld et al. (2016, 2017). Given the lack of M4 and M5 stars in the Kraus et al. (2008) sample, we restrict our comparison of companion fractions to systems with primary spectral types of M3 or earlier. With this restriction, the spectral types of the two samples are consistent with being drawn from the same distribution, with a p-value of 0.17, according to the χ^2 test implemented with the *R Project for Statistical Computing* (R Development Core Team 2008). This result is independent of how the spectral types are categorically binned.

We note that, while similar techniques were used to observe the disk and comparison samples, different observing conditions may have led to discrepancies in the sensitivity to companions between the two samples. In addition, literature data that did not include aperture masking were used for several systems in the disk sample, reducing our sensitivity to close-in companions relative to the comparison sample. We estimate below the number of companions this may have caused us to miss in the disk sample.

Our aim in this study was to determine whether the fraction of disk systems with a stellar companion is lower than that of systems without disks. Thus, to compare survey completeness, we estimated the number of companions detected in diskless systems which would have been missed if they existed with the same brightness and separation around stars in the disk sample. Figure 8 shows the limiting magnitude as a function of separation of the disk systems for which no companion was found. Also plotted are the magnitudes and separations of the companions found in the diskless sample for systems with primary spectral type M3 or earlier. The majority of these companions would have been detected had they existed around the stars in our disk sample. The companions that may have been missed were found using aperture masking by Kraus et al. (2008). Our sensitivities to these close-in sources are lower for

a number of stars in our sample due to masking data not being available, calibration issues due to data being taken in position angle mode, and tip-tilt correction problems (see Section 2). For example, 2MASS J16142029-1906481 was observed without masking by Lafrenière et al. (2014). If the 75 systems in the diskless sample had been observed with the same sensitivity achieved for this source, companions detected by Kraus et al. (2008) would have been missed in 14 systems, equal to 19% of the diskless sample. If 2MASS J16142029-1906481 followed the same underlying companion probability distribution as the diskless sample, we would thus have expected to miss 0.19 companions on average. Similarly, our observations of 2MASS J16103956-1916524, which suffered from poor tip-tilt correction, would not have detected five companions from the diskless sample for an expected value of 0.07 companions missed. The fraction of Kraus et al. (2008) companions in systems without disks that would have been missed in our disk sample can be calculated in this manner for each star in the sample. With this calculation, we found that even if systems with and without disks shared the same distribution of companion brightnesses and separations, we would have only expected to not detect approximately two to three companions in the disk sample due to lower sensitivities. Restricting ourselves to the primordial disks in our sample, we would have expected to miss fewer than one companion relative to the diskless sample.

With this caveat in mind, we now compare the companion fractions of Upper Sco systems with and without disks. For spectral types M3 and earlier, 35 out of 75 stars without disks have at least one companion. By contrast, only seven out of 50 systems with disks include companions. From the Fisher Exact Test, the probability that the lower companion fraction in star–disk systems is due to chance is 2×10^{-4}. Even if our previous estimate of three missed companions were added to the total

number of companions observed around stars with disks, the Fisher Exact Test would still give a probability of 2×10^{-3} that the companion fractions are the same for stars with and without disks. Since this includes the debris/evolved transitional disks and we are primarily concerned with the evolution of primordial disks, we eliminated the potential debris disks and repeated the comparison. We found that six of the 26 primordial disk systems with spectral types M3 and earlier host companions, giving a p-value of 0.04 when compared to the stars without disks. Thus, the fraction of multiple systems among stars with primordial disks is lower than that of stars without disks with marginal significance.

Kuruwita et al. (2018) have also studied the effect of binarity on the presence of disks in Upper Sco in a radial velocity search for stellar companions to 55 Upper Sco G, K, and M stars with an infrared excess. The authors find a stellar companion fraction for these systems of $0.06^{+0.07}_{-0.02}$ for periods less than 20 yr. This is lower than the fraction expected for field stars with the same primary mass distribution, $0.12^{+0.02}_{-0.01}$, although the fractions agree within uncertainties. This survey probes separations within $\sim0\rlap{.}{''}05$ at the ~145 pc distance of Upper Sco, separations similar to and within the inner working angle of our current aperture masking observations. Thus, it would be possible with a larger radial-velocity sample to test if the lower companion fraction in systems with disks relative to those without disks found in the present study holds for closer-separation companions. Such a sample was recently provided by Esplin et al. (2018), who compiled an updated census of 484 Upper Sco disks identified by infrared excess.

4.3. 2MASS J16075796-2040087: An Accreting Circumbinary Disk

While the majority of the disks in the Upper Sco multiple systems in our sample appear to be located around a single star within each system, the disk in 2MASS J16075796-2040087 is likely to be circumbinary. This system has a stellar companion at a projected separation of 6.3 au and a disk with 880 μm flux density of 23.49 mJy, one of the brighter millimeter sources in the present sample. Corrected for the updated Gaia distance to this system in Table 1, Barenfeld et al. (2017) found that the dust disk in this system extends to 15 ± 1 au while the gas component reaches to 46^{+6}_{-2} au, well beyond the projected companion separation. While it is possible that the physical separation of the components of this system is wider than their projected separation, it would have to be over a factor of seven larger to be outside of the gas disk. Harris et al. (2012) constructed the probability distribution for the ratio of physical to projected separation of a binary using a Monte Carlo simulation of the underlying orbital parameters. Depending on the assumed priors for orbital parameters, the distribution peaks between a ratio of 0.5 and 1.5, with only a low probability tail extending beyond a ratio of 3. 2MASS J16075796-2040087 is therefore most likely to be a circumbinary disk.

However, in Figure 6, there is a strong infrared excess at wavelengths as short as 1.7 μm, indicating the presence of hot dust close to one or both of the stars. We note that the stellar photospheric emission calculated for this system assumes a spectral type of M1 (Luhman & Mamajek 2012), while the primary star may have an earlier spectral type (see Kraus & Hillenbrand 2009; Cody et al. 2017). Despite the uncertainty in the stellar photosphere, it is clear that there is significant circumstellar material around at least one of the stars in this

system. Kraus & Hillenbrand (2009) found that there is likely to be an accretion-powered outflow based on strong optical emission lines, while Cody et al. (2017) observed bursting behavior on a ~15 day timescale in the optical light curve, consistent with episodic accretion.

One possible explanation for these observations is that material from the inner edge of the circumbinary disk is streaming across the dynamically cleared inner gap and accreting onto one or both of the stars (e.g., Artymowicz & Lubow 1996; Günther & Kley 2002). The details of this process depend strongly on the mass ratio and orbital parameters of the binary, but it is generally expected that this accretion will be modulated with a period of order that of the binary orbit (Muñoz & Lai 2016). Modulated accretion has been observed in spectroscopic binaries with circumbinary disks such as DQ Tau (Mathieu et al. 1997), UZ Tau E (Jensen et al. 2007), and TWA 3A (Tofflemire et al. 2017a, 2017b). However, 2MASS J16075796-2040087 exhibits optical variability on a ~15 day timescale, much shorter than the orbital period of a binary with a projected separation of 4.6 au. Direct accretion onto the stars in the binary is only expected for spectroscopic binaries with separations of a fraction of an au. In wider systems, inner circumprimary and circumsecondary disks are expected to be fed and maintained by the streams (Günther & Kley 2002; Dutrey et al. 2016). Observations of GG Tau (Dutrey et al. 1994, 2014), with a projected separation of ~35 au, UY Aur (Close et al. 1998; Duvert et al. 1998; Tang et al. 2014), ~125 au, and L1551 (Takakuwa et al. 2014), ~70 au, fit such a scenario. A similar process may be taking place in 2MASS J16075796-2040087. Though the 4.6 au binary separation makes this system an intermediate case between spectroscopic binaries and wider pairs such as GG Tau, a circumprimary and/or circumsecondary disk replenished by streams from the outer circumbinary disk may be present. Accretion from the inner disk(s) may then be causing the observed optical emission lines, infrared excess, and variability on timescales unrelated to the binary orbital period.

5. Discussion

In this section we investigate how the relationship between disks and stellar companions varies with age. We compare the fractions of disk systems with close companions and examine the relationship between companion separation and disk millimeter luminosity in the 1–2 Myr old Taurus and 5–11 Myr old Upper Sco regions. We then discuss the implications of these results for disk evolution.

5.1. Companion Frequency of Disk Systems in Taurus and Upper Sco

Studies of how disks are affected by stellar companions in Taurus and other young star-forming regions have shown that multiplicity has a significant impact during the first 1–2 Myr of disk evolution. The infrared-detected disk fraction of 1–2 Myr old stars with close companions ($\leqslant40$ au separation) is lower by approximately a factor of two to three than that of single stars of the same age (Cieza et al. 2009; Kraus et al. 2012; Cheetham et al. 2015). In Upper Sco (age 5–11 Myr), infrared-detected disks are also less frequent for systems with a close companion than for single stars, but by approximately the same factor of two to three seen for 1–2 Myr old systems (Kraus et al. 2012). This suggests that after the first 1–2 Myr of a
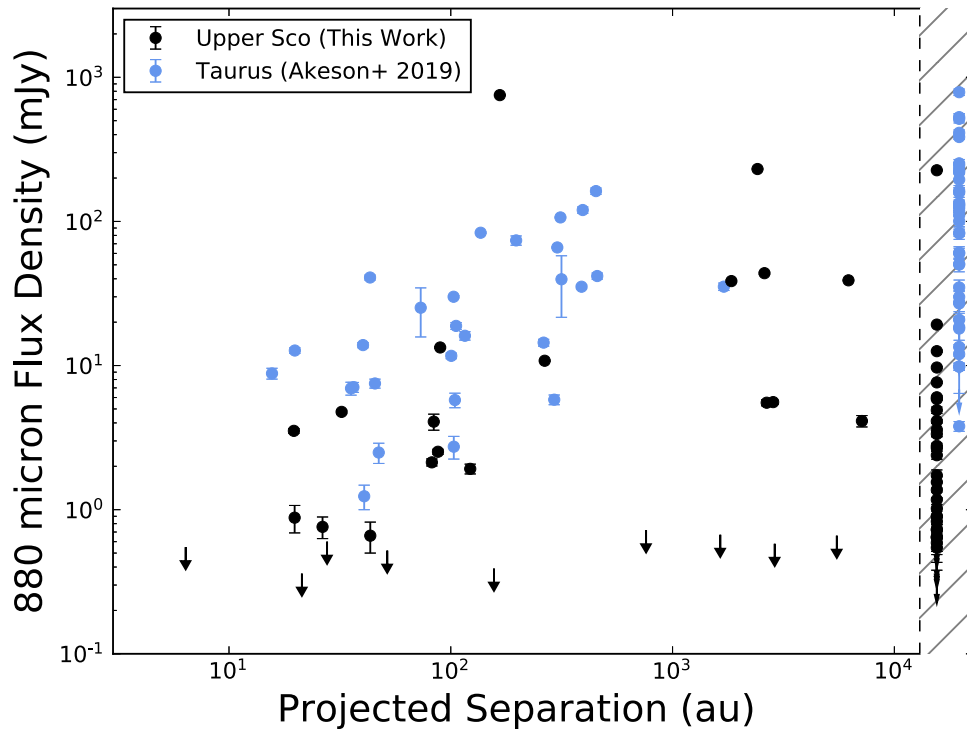
Figure 9. Total 880 μm continuum flux density and project companion separations of Upper Sco systems with primordial disks. Flux densities have been scaled to a common distance of 145 pc. Single stars are shown in the hatched region to the right of the figure. Taurus systems from Akeson et al. (2019) are shown in blue. Unlike in Taurus, where disks are significantly fainter in systems with companions, the brightness distributions of disks in systems with and without companions are indistinguishable in Upper Sco.

disk's evolution, the presence of a companion has no further effect on disk frequency as traced by dust infrared emission.

We tested the effect of stellar companions on disks between the ages of Taurus and Upper Sco using the expanded sample of Upper Sco binaries presented in this work. Our sample was specifically chosen to include Upper Sco systems with infrared-detected disks. Due to this selection criterion, we could not compare the disk frequencies of close binaries to that of single stars. Instead, we compared the fraction of close companions among systems with disks in Taurus and Upper Sco. Of the 83 Taurus G, K, and M stars with infrared-detected disks listed in Kraus et al. (2012) that have been surveyed for companions, 13 host a stellar companion within a projected separation of 40 au. In the present Upper Sco survey, we find 11 stars with such companions among the 82 primordial infrared-detected disks in our sample. These close companion fractions are consistent according to the Fisher exact test, with a p-value of 0.83. This supports the Kraus et al. (2012) result that stellar companions have little to no effect on disk evolution as traced by infrared-emitting dust after the first 1–2 Myr. Instead, the lower companion fraction for systems with infrared-detected disks in Upper Sco relative to those without disks (Section 4.2) is simply due to the reduction in the disk fraction of multiple systems that occurs before an age of 1–2 Myr.

5.2. Millimeter Emission and Multiplicity

Harris et al. (2012) found a clear relationship between companion separation and disk millimeter luminosity in Taurus multiple systems. Taurus disks in systems with projected companion separations between 30 and 300 au are fainter by a factor of five than those in single-star and wider-companion systems, while disks in systems with companions projected

within 30 au are an additional factor of five fainter. We now use the current sample to test this relationship in Upper Sco and compare the results to Taurus.

Our goal was to isolate the effect of binarity on disk evolution. For Upper Sco, we used the Upper Sco primordial disk systems in the current sample with ALMA 0.88 mm continuum flux density measurements from Barenfeld et al. (2016). For Taurus, we used the compilation of 1.3 millimeter flux densities of infrared-identified Class II Taurus systems from Akeson et al. (2019) and selected systems classified as primordial disks by Luhman et al. (2010). Flux densities, originally measured by Andrews et al. (2013), Akeson & Jensen (2014), Ward-Duong et al. (2018), and Akeson et al. (2019), have been scaled to 0.88 mm using the scaling factor of 2.55 assumed for Taurus disks by Andrews et al. (2013). We restricted the Taurus sample to systems with single or primary stellar mass between 0.14 $M_\odot$ and 1.7 $M_\odot$ to match the stellar mass range of the Upper Sco sample (Barenfeld et al. 2016). Within this range, 78% of Taurus systems in our final comparison sample have a single star or primary stellar mass below 0.6 $M_\odot$, compared to 87% of Upper Sco systems. We note, however, that the Upper Sco sample is skewed toward slightly lower stellar masses than that of Taurus, with 69% of systems <0.3 $M_\odot$ compared to 24% in Taurus. For both samples, we excluded triple and higher-order systems in order to isolate the effect of a single companion separation. We also excluded circumbinary disks to focus on the effects of disk truncation by an external companion.

Figure 9 shows the 0.88 mm continuum flux densities of the binary and single systems in the Taurus and Upper Sco samples defined above. Flux densities have been scaled to a common distance of 145 pc. Binaries are divided into systems with separation <300 au and >300 au, with flux densities representing
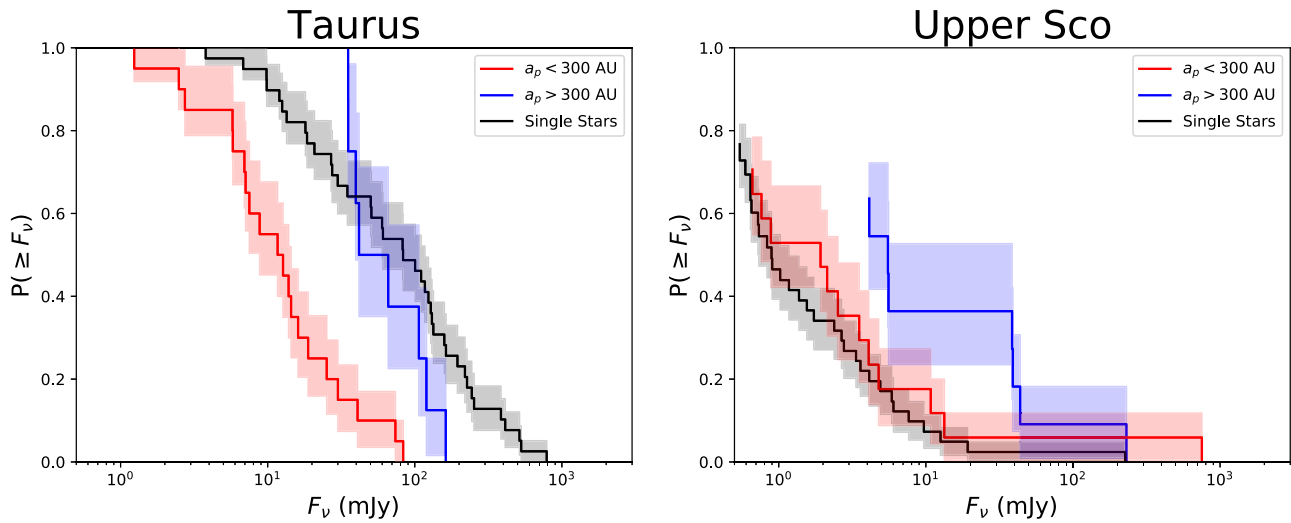
Figure 10. Cumulative distributions of 880 μm continuum flux density for the Taurus (left) and Upper Sco (right) systems shown in Figure 9, calculated using the Kaplan–Meier product-limit estimator. Flux densities have been scaled to a common distance of 145 pc. In the case of Upper Sco, the distribution is only shown to the flux density of the faintest detection. Below this, the assumptions of the Kaplan–Meier product-limit estimator are violated, as all sources are upper limits. In Taurus, single stars are significantly brighter than systems with companions within a projected separation of 300 au. In Upper Sco, however, the brightnesses are similar.

the total emission of both components, following Harris et al. (2012). We note that the Taurus and Upper Sco samples contain only eight and 11 systems, respectively, with separation >300 au. The flux density distinction between single stars and binaries separated by <300 au observed in Taurus is not present in Upper Sco. The difference is clearly apparent in Figure 10, which shows the cumulative flux distributions of single stars, systems with a companion beyond 300 au, and systems with a companion within 300 au. These distributions were calculated using the Kaplan–Meier product-limit estimator to account for the sources without a millimeter detection.

In the case of Taurus, the flux distributions of systems with companions beyond 300 au and single-star systems are statistically indistinguishable, with p-values of 0.50 and 0.79 given by the log-rank and Peto & Peto Generalized Wilcoxian two-sample tests, implemented in R. The brightnesses of the systems with companions within 300 au are clearly lower, however. The log-rank and Peto & Peto Generalized Wilcoxian two-sample tests give p-values of 7.36×10^{-5} and 4.22×10^{-5} that these systems are drawn from the same brightness distribution as single stars. These results are consistent with those originally found by Harris et al. (2012; see also Akeson et al. 2019). We note that when comparing disk millimeter brightnesses, the observed correlation between disk brightness and stellar mass (Andrews et al. 2013; Carpenter et al. 2014; Ansdell et al. 2016, 2017; Barenfeld et al. 2016; Pascucci et al. 2016), must be taken into account. We find that the distributions of Taurus single-star masses and primary masses for binaries with a separation of <300 au are statistically consistent with p-values of 0.69 and 0.62 given by the two versions of the Anderson–Darling test, implemented in R. Therefore, the comparison of the disk luminosity distributions in these two samples are not affected by stellar mass bias.

For Upper Sco, the measured flux densities for single stars, wide companions, and close companions are all shifted to lower fluxes relative to Taurus. As with Taurus, the single-star and >300 au separation companion flux distributions are indistinguishable, with p-values of 0.43 and 0.10 given by the two-sample tests, although the sample size of wide companions is small. In contrast to Taurus, however, the flux distribution of <300 au companion systems is consistent with that of single

stars in Upper Sco, with p-values of 0.85 and 0.62. As is the case for Taurus, stellar mass does not influence this result; the stellar mass distributions of Upper Sco stars with and without companions within 300 au are consistent, with p-values of 0.75 and 0.73. Thus, it appears that while young disks in Taurus are strongly influenced by the presence of stellar companions, by the 5–11 Myr age of Upper Sco disk evolution has proceeded in such a way as to erase these initial effects.

In Figure 11, we compare the ^{12}CO $J = 3$–2 integrated line flux and projected separation for the Upper Sco primordial disks in binary systems. Figure 12 shows the cumulative flux distributions, calculated using the Kaplan–Meier estimator as above. Both figures show similar CO flux distributions for single stars and systems with companions at CO fluxes greater than $0.5 \, \mathrm{Jy \, km \, s^{-1}}$, independent of companion separation. However, none of the 14 systems with a companion within 300 au and CO flux below $0.5 \, \mathrm{Jy \, km \, s^{-1}}$ are detected in CO, while 11 of the 37 such single stars are detected. The Kaplan–Meier estimator is not reliable below $0.5 \, \mathrm{Jy \, km \, s^{-1}}$ due to the lack of detections in the former 14 systems. Therefore, the effects of binarity on gas and dust in disks may be different in Upper Sco. It is difficult to precisely quantify any such difference, however, as a 20% reduction in the CO flux of these single systems would result in only three being detected, while a 30% reduction would lead to none being detected. Thus, the lack of CO detections below $0.5 \, \mathrm{Jy \, km \, s^{-1}}$ in multiple systems may be due to only a small difference in flux. Higher-sensitivity observations are necessary to definitively determine whether a difference exists in the CO integrated fluxes of disks with and without companions.

5.3. Stellar Companions and Disk Evolution

The observed correlation between the radial extent of millimeter-emitting grains and disk millimeter luminosity (Barenfeld et al. 2017; Tripathi et al. 2017) suggests that the results of Section 5.2 can be explained by the evolution of dust disk sizes in single and multiple systems. Disks in binary systems that are initially truncated by a stellar companion and survive to an age of 1–2 Myr will be smaller in size than their counterparts in single-star systems. These truncated disks will
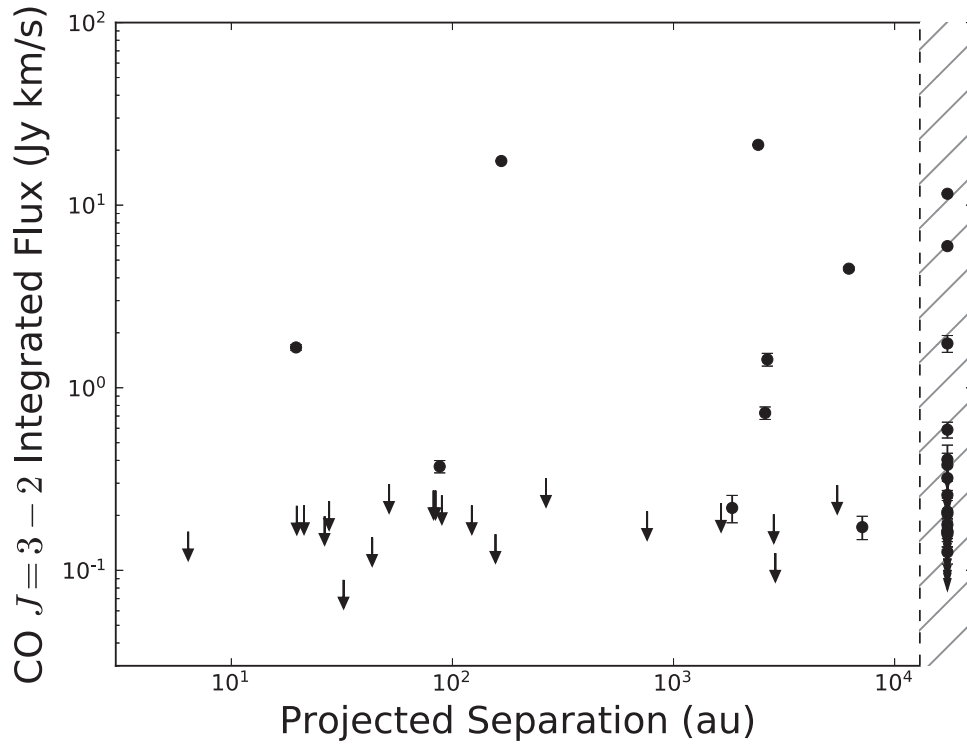
Figure 11. CO $J = 3$–2 integrated line fluxes vs. projected companion separations of Upper Sco systems with disks. Fluxes have been scaled to a common distance of 145 pc. Single stars are shown in the hatched region to the right of the figure. Although the distributions of fluxes for the single stars and systems with companions within 300 au are statistically indistinguishable, 11 out of 37 single-star systems with fluxes below 0.5 Jy km s^{-1} are detected, compared to none of the 14 such systems with companions separated by less than 300 au.
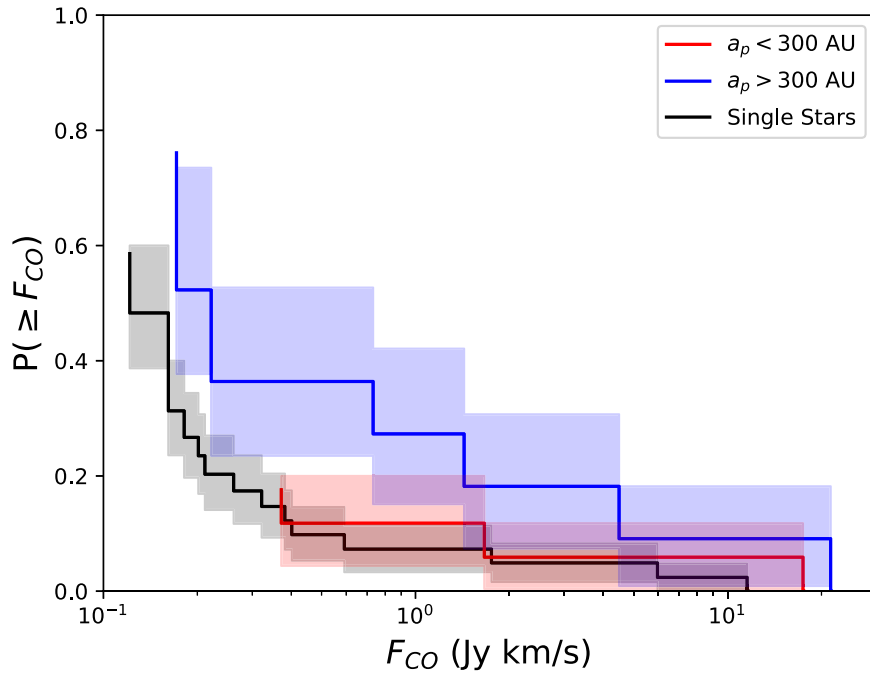
Figure 12. Cumulative distributions of the CO $J = 3$–2 integrated line fluxes of Upper Sco systems with disks, calculated using the Kaplan–Meier product-limit estimator. Fluxes have been scaled to a common distance of 145 pc. The distribution is only shown to the flux of the faintest detection. Below this, the assumptions of the Kaplan–Meier product-limit estimator are violated, as all sources are upper limits. The log-rank and Peto & Peto Generalized Wilcoxian two-sample tests cannot distinguish between the flux distributions of single stars and systems with a companion within a projected separation of 300 au.

thus be fainter, as is seen in Taurus (Harris et al. 2012; Akeson et al. 2019). A surface brightness comparison of disks in Taurus binary systems with those around single stars could measure the extent to which lower flux densities of binary system disks are due to this loss of the outer disk.

Barenfeld et al. (2017) measured the sizes of dust disks in Upper Sco, finding that these disks are smaller than younger systems by a factor of ~3 on average. This suggests that the population of millimeter-sized grains in the outer disk is lost as disks evolve, providing a natural explanation for the similar

luminosity distributions of disks in single and multiple systems in Upper Sco. Dust disks in multiple systems are truncated by their stellar companions, but their subsequent evolution is not as strongly affected by the presence of the companion after an age of 1–2 Myr, as shown in Section 5.1. Conversely, the outside-in evolution of single-star disks effectively allows them to "catch-up" to the smaller sizes of disks in multiple systems by an age of 5–11 Myr. The end result of dust disks tens of au in size with similar millimeter brightnesses is the same regardless of the presence or absence of a stellar companion.

Gorti et al. (2015) have modeled disk evolution under the effects of viscous accretion, photoevaporation, dust radial migration, and dust growth and fragmentation, finding that the radial extent of millimeter-sized dust grains is expected to decline over time due to migration. The resulting millimeter dust disk sizes are similar to those measured for Upper Sco by Barenfeld et al. (2017). In this scenario, millimeter-sized grains from the outer disk replenish some of the dust lost from the inner disk due to viscous accretion, so that at the age of Upper Sco the inner disk is all that remains. However, disks in binary systems would lack this outer reservoir of millimeter-emitting grains due to tidal truncation, preventing the inner disk from being replenished. This scenario would result in disks in binaries being fainter than disks in single systems, in contrast to what is observed in Section 5.2. Thus, the shrinking of dust disks around single stars cannot simply be due to millimeter grains migrating inwards and remaining observable in the inner disk.

In addition to depletion through migration, the models of Gorti et al. (2015) predict that millimeter-sized grains will also be depleted in the outer disk through fragmentation. As photoevaporation lowers the density of gas in the outer disk, collisional velocities of millimeter dust grains will increase, leading to fragmentation into smaller grains that are not detectable at millimeter wavelengths. If this process occurs on a more rapid timescale than radial migration, it could provide a mechanism to remove outer disk millimeter grains without transporting them to the inner disk. Dust disks would therefore shrink in size without replenishment of the inner disk, resulting in disks having the same millimeter brightnesses in multiple and single systems.

On the other hand, local gas pressure maxima in disks are expected to trap concentrations of dust that would appear optically thick at millimeter wavelengths (e.g., Whipple 1972; Pinilla et al. 2012). Optically thick dust substructure formed in this way has been suggested as an explanation of the observed correlation between dust disk size and millimeter luminosity seen in Taurus (Tripathi et al. 2017) and Upper Sco (Barenfeld et al. 2017). If millimeter grains in the inner disk are confined by dust traps to optically thick, unresolved substructures, dust could migrate into the inner disk without increasing its observed luminosity. Disks around single stars in Upper Sco would thus have higher dust masses than disks in multiple systems, but this extra material would be hidden by optical depth effects, causing single and multiple system disks to have the same millimeter brightnesses.

6. Summary

We have conducted a census of stellar companions around 112 stars with disks in the Upper Scorpius OB Association. Combining new observations with results from the literature, we find 30 sources brighter than $K = 15$ and with separations of less than $2''$ from the target stars in 27 systems. These objects are likely to be companions based on the expected density of field stars. We compared the companion fraction of this sample to that of Upper Sco systems without disks (Kraus et al. 2008) and investigated how the millimeter properties of these disks depend on companion separation. The key conclusions of this paper are as follows.

1. ALMA images of the systems with disks and companions show that, for most such systems, the dust continuum emission is located around the primary or companion individually or is not detected toward either. For the systems with unresolved continuum emission encompassing both primary and companion, infrared SEDs show evidence for warm dust around one or both individual stars in the system.

2. Of the 50 primordial and debris/evolved transitional disk-hosting stars with spectral types G0-M3 in our sample, only seven have stellar companions brighter than $K = 15$ with separations less than $2''$. Thirty-five systems in a comparison sample of 75 Upper Sco stars without disks in this spectral type range have stellar companions meeting the same brightness and separation criteria. The companion fraction for stars with disks is significantly lower, with a p-value of 2×10^{-4}. Restricting this comparison to primordial disks, we find that six of 26 stars with disks have a companion, a marginally lower fraction than that for stars without disks, with a p-value of 0.04.

3. The fraction of Upper Sco disk systems with a companion within 40 au is consistent with that of Taurus disks. While external stellar companions disrupt the early phases in disk evolution, as manifested in the lower disk fraction for close multiple systems than for single stars in Taurus, subsequent evolution appears to be dominated by internal disk processes.

4. The observed distribution of millimeter continuum luminosity in Upper Sco is the same for disks in single-star systems and systems with a companion within a projected separation of 300 au. In contrast, disks in younger Taurus systems with such companions are fainter than those in single systems (Harris et al. 2012; Akeson et al. 2019), likely due to the smaller sizes of disks truncated by a stellar companion. This suggests that dust disks evolve from the outside-in between the ages of Taurus and Upper Sco, such that disks around single stars match the sizes and millimeter brightnesses of disks in binary systems by the 5–11 Myr age of Upper Sco.

ORCID iDs

Scott A. Barenfeld https://orcid.org/0000-0001-5222-6851
John M. Carpenter https://orcid.org/0000-0003-2251-0602
Aaron C. Rizzuto https://orcid.org/0000-0001-9982-1332
Adam L. Kraus https://orcid.org/0000-0001-9811-568X
Tiffany Meshkat https://orcid.org/0000-0001-6126-2467
Rachel L. Akeson https://orcid.org/0000-0001-9674-1564
Eric L. N. Jensen https://orcid.org/0000-0002-4625-7333
Sasha Hinkley https://orcid.org/0000-0001-8074-2562

References

Akeson, R. L., & Jensen, E. L. N. 2014, ApJ, 784, 62
Akeson, R. L., Jensen, E. L. N., Carpenter, J., et al. 2019, ApJ, 872, 158
Alexander, R., Pascucci, I., Andrews, S., Armitage, P., & Cieza, L. 2014, in Protostars and Planets VI, ed. H. Beuther et al. (Tucson, AZ: Univ. Arizona Press), 475
Amara, A., & Quanz, S. P. 2012, MNRAS, 427, 948
Andrews, S. M., Rosenfeld, K. A., Kraus, A. L., & Wilner, D. J. 2013, ApJ, 771, 129
Ansdell, M., Williams, J. P., & Cieza, L. A. 2015, ApJ, 806, 221
Ansdell, M., Williams, J. P., Manara, C. F., et al. 2017, AJ, 153, 240
Ansdell, M., Williams, J. P., van der Marel, N., et al. 2016, ApJ, 828, 46
Artymowicz, P., & Lubow, S. H. 1994, ApJ, 421, 651
Artymowicz, P., & Lubow, S. H. 1996, ApJL, 467, L77
Bailer-Jones, C. A. L., Rybizki, J., Fouesneau, M., Mantelet, G., & Andrae, R. 2018, AJ, 156, 58
Baraffe, I., Chabrier, G., Allard, F., & Hauschildt, P. H. 2002, A&A, 382, 563
Barenfeld, S. A., Carpenter, J. M., Ricci, L., & Isella, A. 2016, ApJ, 827, 142
Barenfeld, S. A., Carpenter, J. M., Sargent, A. I., Isella, A., & Ricci, L. 2017, ApJ, 851, 85
Bergfors, C., Brandner, W., Janson, M., et al. 2010, A&A, 520, A54
Birnstiel, T., & Andrews, S. M. 2014, ApJ, 780, 153
Borucki, W. J., Koch, D., Basri, G., et al. 2010, Sci, 327, 977
Bouwman, J., Lawson, W. A., Dominik, C., et al. 2006, ApJL, 653, L57
Bouy, H., Martín, E. L., Brandner, W., et al. 2006, A&A, 451, 177
Bradley, L., Sipocz, B., Robitaille, T., et al. 2016, Photutils: Photometry tools, Astrophysics Source Code Library, ascl:1609.011
Brauer, F., Dullemond, C. P., Johansen, A., et al. 2007, A&A, 469, 1169
Carpenter, J. M. 2002, AJ, 124, 1593
Carpenter, J. M., Hillenbrand, L. A., & Skrutskie, M. F. 2001, AJ, 121, 3160
Carpenter, J. M., Mamajek, E. E., Hillenbrand, L. A., & Meyer, M. R. 2006, ApJL, 651, L49
Carpenter, J. M., Ricci, L., & Isella, A. 2014, ApJ, 787, 42
Chabrier, G., Baraffe, I., Allard, F., & Hauschildt, P. 2000, ApJ, 542, 464
Chabrier, G., Johansen, A., Janson, M., & Rafikov, R. 2014, in Protostars and Planets VI, ed. H. Beuther et al. (Tucson, AZ: Univ. Arizona Press), 619
Cheetham, A. C., Kraus, A. L., Ireland, M. J., et al. 2015, ApJ, 813, 83
Chen, X., Arce, H. G., Zhang, Q., et al. 2013, ApJ, 768, 110
Cieza, L. A., Padgett, D. L., Allen, L. E., et al. 2009, ApJL, 696, L84
Close, L. M., Dutrey, A., Roddier, F., et al. 1998, ApJ, 499, 883
Cody, A. M., Hillenbrand, L. A., David, T. J., et al. 2017, ApJ, 836, 41
Cutri, R. M., Skrutskie, M. F., van Dyk, S., et al. 2003, yCat, 2246
Daemgen, S., Elliot Meyer, R., Jayawardhana, R., & Petr-Gotzens, M. G. 2016, A&A, 586, A12
Dupuy, T. J., Kratter, K. M., Kraus, A. L., et al. 2016, ApJ, 817, 80
Dutrey, A., Di Folco, E., Beck, T., & Guilloteau, S. 2016, A&A, 24, 5
Dutrey, A., di Folco, E., Guilloteau, S., et al. 2014, Natur, 514, 600
Dutrey, A., Guilloteau, S., & Simon, M. 1994, A&A, 286, 149
Duvert, G., Dutrey, A., Guilloteau, S., et al. 1998, A&A, 332, 867
Eisner, J. A., Hillenbrand, L. A., White, R. J., Akeson, R. L., & Sargent, A. I. 2005, ApJ, 623, 952
Esplin, T. L., Luhman, K. L., Miller, E. B., & Mamajek, E. E. 2018, AJ, 156, 75
Fischer, D. A., & Marcy, G. W. 1992, ApJ, 396, 178
Gaia Collaboration, Brown, A. G. A., Vallenari, A., et al. 2018, A&A, 616, A1
Gaia Collaboration, Prusti, T., de Bruijne, J. H. J., et al. 2016, A&A, 595, A1
Ghez, A. M., Neugebauer, G., & Matthews, K. 1993, AJ, 106, 2005
Girardi, L., Groenewegen, M. A. T., Hatziminaoglou, E., & da Costa, L. 2005, A&A, 436, 895
Gomez Gonzalez, C. A., Wertz, O., Absil, O., et al. 2017, AJ, 154, 7
Gorti, U., Hollenbach, D., & Dullemond, C. P. 2015, ApJ, 804, 29
Günther, R., & Kley, W. 2002, A&A, 387, 550
Harris, R. J., Andrews, S. M., Wilner, D. J., & Kraus, A. L. 2012, ApJ, 751, 115
Hartmann, L., Calvet, N., Gullbring, E., & D'Alessio, P. 1998, ApJ, 495, 385
Helled, R., Bodenheimer, P., Podolak, M., et al. 2014, in Protostars and Planets VI, ed. H. Beuther et al. (Tucson, AZ: Univ. Arizona Press), 643
Hernández, J., Hartmann, L., Calvet, N., et al. 2008, ApJ, 686, 1195
Hirsch, L. A., Ciardi, D. R., Howard, A. W., et al. 2017, AJ, 153, 117
Holman, M. J., & Wiegert, P. A. 1999, AJ, 117, 621
Jang-Condell, H. 2015, ApJ, 799, 147
Jensen, E. L. N., Dhital, S., Stassun, K. G., et al. 2007, AJ, 134, 241
Jensen, E. L. N., Mathieu, R. D., & Fuller, G. A. 1994, ApJL, 429, L29
Jensen, E. L. N., Mathieu, R. D., & Fuller, G. A. 1996, ApJ, 458, 312
Köhler, R., Kunkel, M., Leinert, C., & Zinnecker, H. 2000, A&A, 356, 541
Kohler, R., & Leinert, C. 1998, A&A, 331, 977
Kraus, A. L., & Hillenbrand, L. A. 2007, ApJ, 664, 1167
Kraus, A. L., & Hillenbrand, L. A. 2009, ApJ, 704, 531
Kraus, A. L., & Hillenbrand, L. A. 2012, ApJ, 757, 141
Kraus, A. L., Ireland, M. J., Hillenbrand, L. A., & Martinache, F. 2012, ApJ, 745, 19
Kraus, A. L., Ireland, M. J., Huber, D., Mann, A. W., & Dupuy, T. J. 2016, AJ, 152, 8

Kraus, A. L., Ireland, M. J., Martinache, F., & Hillenbrand, L. A. 2011, ApJ, 731, 8
Kraus, A. L., Ireland, M. J., Martinache, F., & Lloyd, J. P. 2008, ApJ, 679, 762
Kuruwita, R. L., Ireland, M., Rizzuto, A., Bento, J., & Federrath, C. 2018, MNRAS, 480, 5099
Lafrenière, D., Jayawardhana, R., Brandeker, A., Ahmic, M., & van Kerkwijk, M. H. 2008, ApJ, 683, 844
Lafrenière, D., Jayawardhana, R., van Kerkwijk, M. H., Brandeker, A., & Janson, M. 2014, ApJ, 785, 47
Lee, N., Williams, J. P., & Cieza, L. A. 2011, ApJ, 736, 135
Leinert, C., Zinnecker, H., Weitzel, N., et al. 1993, A&A, 278, 129
Li, Z.-Y., Banerjee, R., Pudritz, R. E., et al. 2014, in Protostars and Planets VI, ed. H. Beuther et al. (Tucson, AZ: Univ. Arizona Press), 173
Lloyd, J. P., Martinache, F., Ireland, M. J., et al. 2006, ApJL, 650, L131
Lohmann, A. W., Weigelt, G., & Wirnitzer, B. 1983, ApOpt, 22, 4028
Long, F., Herczeg, G. J., Pascucci, I., et al. 2018, ApJ, 863, 61
Luhman, K. L., Allen, P. R., Espaillat, C., Hartmann, L., & Calvet, N. 2010, ApJS, 186, 111
Luhman, K. L., Herrmann, K. A., Mamajek, E. E., Esplin, T. L., & Pecaut, M. J. 2018, AJ, 156, 76
Luhman, K. L., & Mamajek, E. E. 2012, ApJ, 758, 31
Martinache, F., Lloyd, J. P., Ireland, M. J., Yamada, R. S., & Tuthill, P. G. 2007, ApJ, 661, 496
Mathews, G. S., Williams, J. P., Ménard, F., et al. 2012, ApJ, 745, 23
Mathieu, R. D., Stassun, K., Basri, G., et al. 1997, AJ, 113, 1841
Mawet, D., Milli, J., Wahhaj, Z., et al. 2014, ApJ, 792, 97
Metchev, S. A., & Hillenbrand, L. A. 2009, ApJS, 181, 62
Muñoz, D. J., & Lai, D. 2016, ApJ, 827, 43
Nuernberger, D., Chini, R., & Zinnecker, H. 1997, A&A, 324, 1036
Owen, J. E., Clarke, C. J., & Ercolano, B. 2012, MNRAS, 422, 1880
Papaloizou, J., & Pringle, J. E. 1977, MNRAS, 181, 441
Pascucci, I., Testi, L., Herczeg, G. J., et al. 2016, ApJ, 831, 125
Pichardo, B., Sparke, L. S., & Aguilar, L. A. 2005, MNRAS, 359, 521
Pinilla, P., Birnstiel, T., Ricci, L., et al. 2012, A&A, 538, A114

Pravdo, S. H., Shaklan, S. B., Wiktorowicz, S. J., et al. 2006, ApJ, 649, 389
Raghavan, D., McAlister, H. A., Henry, T. J., et al. 2010, ApJS, 190, 1
Ratzka, T., Köhler, R., & Leinert, C. 2005, A&A, 437, 611
R Development Core Team 2008, R: A language and environment for statistical computing (Vienna: R Foundation for Statistical Computing), http://www.R-project.org.
Readhead, A. C. S., Nakajima, T. S., Pearson, T. J., et al. 1988, AJ, 95, 1278
Roeser, S., Demleitner, M., & Schilbach, E. 2010, AJ, 139, 2440
Service, M., Lu, J. R., Campbell, R., et al. 2016, PASP, 128, 095004
Skrutskie, M. F., Cutri, R. M., Stiening, R., et al. 2006, AJ, 131, 1163
Soummer, R., Pueyo, L., & Larkin, J. 2012, ApJL, 755, L28
Takakuwa, S., Saito, M., Saigo, K., et al. 2014, ApJ, 796, 1
Tang, Y.-W., Dutrey, A., Guilloteau, S., et al. 2014, ApJ, 793, 10
Testi, L., Birnstiel, T., Ricci, L., et al. 2014, in Protostars and Planets VI, ed. H. Beuther et al. (Tuson, AZ: Univ. Arizona Press), 339
Tofflemire, B. M., Mathieu, R. D., Ardila, D. R., et al. 2017a, ApJ, 835, 8
Tofflemire, B. M., Mathieu, R. D., Herczeg, G. J., Akeson, R. L., & Ciardi, D. R. 2017b, ApJL, 842, L12
Tripathi, A., Andrews, S. M., Birnstiel, T., & Wilner, D. J. 2017, ApJ, 845, 44
Wang, J., Fischer, D. A., Horch, E. P., & Xie, J.-W. 2015a, ApJ, 806, 248
Wang, J., Fischer, D. A., Xie, J.-W., & Ciardi, D. R. 2014a, ApJ, 791, 111
Wang, J., Fischer, D. A., Xie, J.-W., & Ciardi, D. R. 2015b, ApJ, 813, 130
Wang, J., Xie, J.-W., Barclay, T., & Fischer, D. A. 2014b, ApJ, 783, 4
Ward-Duong, K., Patience, J., Bulger, J., et al. 2018, AJ, 155, 54
Weidenschilling, S. J. 1977, MNRAS, 180, 57
Werner, M. W., Roellig, T. L., Low, F. J., et al. 2004, ApJS, 154, 1
Whipple, F. L. 1972, in From Plasma to Planet, ed. A. Evlius (New York: Wiley Interscience), 211
Williams, J. P., Cieza, L. A., Andrews, S. M., et al. 2013, MNRAS, 435, 1671
Wizinowich, P. L., Le Mignant, D., Bouchez, A. H., et al. 2006, PASP, 118, 297
Wright, E. L., Eisenhardt, P. R. M., Mainzer, A. K., et al. 2010, AJ, 140, 1868
Yelda, S., Lu, J. R., Ghez, A. M., et al. 2010, ApJ, 725, 331